

# Brownian Dynamics without Green's Functions

Steven Delong,<sup>1</sup> Florencio Balboa Usabiaga,<sup>2</sup> Rafael Delgado-Buscalioni,<sup>2</sup> Boyce E. Griffith,<sup>3,1</sup> and Aleksandar Donev<sup>1,\*</sup>

<sup>1</sup>*Courant Institute of Mathematical Sciences, New York University, New York, NY 10012*

<sup>2</sup>*Departamento de Física Teórica de la Materia Condensada and Condensed Matter Physics Center (IFIMAC), Universidad Autónoma de Madrid, Madrid 28049, Spain*

<sup>3</sup>*Leon H. Charney Division of Cardiology, Department of Medicine, New York University School of Medicine, New York, NY 10016*

We develop a Fluctuating Immersed Boundary (FIB) method for performing Brownian dynamics simulations of confined particle suspensions. Unlike traditional methods which employ analytical Green's functions for Stokes flow in the confined geometry, the FIB method uses a fluctuating finite-volume Stokes solver to generate the action of the response functions “on the fly”. Importantly, we demonstrate that both the deterministic terms necessary to capture the hydrodynamic interactions among the suspended particles, as well as the stochastic terms necessary to generate the hydrodynamically-correlated Brownian motion, can be generated by solving the steady Stokes equations numerically only once per time step. This is accomplished by including a stochastic contribution to the stress tensor in the fluid equations consistent with fluctuating hydrodynamics. We develop novel temporal integrators that account for the multiplicative nature of the noise in the equations of Brownian dynamics and the strong dependence of the mobility on the configuration for confined systems. Notably, we propose a random finite difference approach to approximating the stochastic drift proportional to the divergence of the configuration-dependent mobility matrix. Through comparisons with analytical and existing computational results, we numerically demonstrate the ability of the FIB method to accurately capture both the static (equilibrium) and dynamic properties of interacting particles in flow.

## I. INTRODUCTION

Stochastic fluctuations in fluids arise from the fact that fluids are composed of molecules whose positions and velocities are random. One can capture thermal fluctuations using direct particle level calculations. But even coarse-grained particle methods [1–3] are computationally expensive because the dynamics of individual particles is much faster than hydrodynamic time scales. Alternatively, thermal fluctuations can be included in the Navier-Stokes equations through stochastic forcing terms, as proposed by Landau and Lifshitz [4]. The basic idea of fluctuating hydrodynamics [5] is to add a stochastic stress tensor to the usual viscous stress tensor [6]. This has been shown to be a very good model of fluids down to essentially molecular scales [3, 7–11].

The presence of suspended particles is a common feature of complex fluids. At small scales, the motion of immersed particles is driven by thermal fluctuations, giving rise to Brownian motion strongly affected by hydrodynamic effects. Fluctuating hydrodynamics has been shown to be a useful tool in modeling the dynamics of colloidal particles and polymer chains suspended in a fluid [12–23]. By coupling a fluctuating fluid solver with immersed particles one can model the Brownian dynamics from the short time scales, at which sound waves play a role [21], to longer times, at which the velocity correlations decay in a power-law manner due to viscous dis-

sipation. At the same time, the dynamics of interest in many problems is the diffusive (Brownian) dynamics of the immersed structures, which happens at much longer times due to the very small Reynolds numbers, or more precisely, the very large Schmidt numbers present in typical applications.

In the limit of zero Reynolds number, or more precisely, infinite Schmidt number, the methods of Brownian [24–30] and Stokesian dynamics [31, 32] have dominated in chemical engineering, and related techniques have been used in biochemical engineering [33–36]. In this work we focus on Brownian dynamics, which can be seen as a simplified version of Stokesian dynamics that does not include second-order multipole terms (rotlets and stresslets) or lubrication effects in the hydrodynamic interactions among the immersed particles. A key common feature of this class of methods is that they simulate the overdamped (diffusive) dynamics of the particles by using Green's functions for steady Stokes flow to capture the effect of the fluid. While this sort of *implicit solvent* approach works very well in many situations, it has several notable technical difficulties: achieving near linear scaling for many-particle systems is technically challenging [28, 30, 31], handling non-trivial boundary conditions (bounded systems) is complicated [29] and has to be done on a case-by-case basis [14, 27, 32, 37, 38], and including Brownian motion requires additional specialized treatment [24, 25]. Notably, combining all components together and performing Brownian or Stokesian dynamics in complex geometry with accurate hydrodynamics, thermal fluctuations, and near-linear scaling requires a rather sophisticated set of tools. This is evidenced by the fact

---

\*Electronic address: donev@courant.nyu.edu

that existing Stokesian dynamics simulations of Brownian suspensions in even the simplest confined geometry, a slit channel, have relied on several uncontrolled approximations [39], even though all of the expressions and tools have, in principle, been developed [37, 40].

At first sight, it may appear that there is a conceptual gap between methods based on fluctuating hydrodynamics and those based on Green’s functions. The fluid inertia, or, more precisely, the momentum diffusion is inherently part of the fluctuating hydrodynamics formulation of Brownian motion [41–44], while it does not appear in the equations of Brownian or Stokesian dynamics. For example, particles suspended in a fluctuating fluid with inertial memory exhibit a well-known power-law decay of the velocity auto-correlation function (VACF) [43], which is not present in Brownian dynamics (BD) because BD is meant to describe longer time scales, at which the VACF looks like a Dirac delta function. In order to access the diffusive scaling, methods based on fluctuating hydrodynamics, such as Lattice-Boltzmann (LB) techniques [16], must ensure that the Schmidt number  $Sc$  is sufficiently large [45], though in practice  $Sc$  is always limited by computational efficiency considerations. Extensive testing has confirmed that with proper care a match can be achieved between results obtained using LB and BD methods [14, 15, 46].

Nevertheless, there remains a gap in the range of accessible Reynolds/Schmidt numbers between the two classes of methods. We close this gap in this work by designing a Fluctuating Immersed Boundary (FIB) method that solves the overdamped (inertia-less) equations of Brownian dynamics using an *explicit solvent* representation of the fluid hydrodynamics. Importantly, the FIB method includes confinement in nontrivial geometries and Brownian motion consistently and with a controlled accuracy, and has linear complexity in the number of immersed particles. The key observation underlying the FIB method is that analytical Green’s functions can be replaced by a steady Stokes solver with a stochastic stress tensor, as dictated by fluctuating hydrodynamics. Specifically, the action of the required response functions (on both deterministic and stochastic terms) is computed “on the fly” rather than pre-computed analytically. The fluid solver can be used to handle nontrivial boundary conditions, including cases where the concentration of chemical reactants affects the fluid flow via osmo-phoretic effects [47, 48]. The stochastic increments required to simulate the Brownian motion are generated by the fluctuating Stokes solver with no additional effort, in arbitrary domains with a combination of standard periodic, no-slip or slip boundaries [49]. Because in confined systems the mobility strongly depends on the positions of the particles relative to the boundaries, we pay special attention to correctly capturing the well-known stochastic drift term proportional to the divergence of the configuration-dependent mobility matrix. In particular, we develop a random finite difference approach that is related, but distinct from, the traditional Fixman midpoint method.

Rather closely related to our proposal is the work on the Stochastic Immersed Boundary Method (SIBM) and its generalization the Stochastic Eulerian Lagrangian Method (SELM) developed by Atzberger and collaborators [17, 50], as well as the work of Maxey and collaborators on the Force Coupling Method (FCM) [51–53]. In work independent from ours, Keaveny has recently included thermal fluctuations in the fluctuating FCM method [20], and also accounted for stresslet and rotlet terms (which are not included in our FIB method). While inertia can be included easily in both SELM and FCM, as it can be in the Inertial Coupling Method (ICM) [19] very closely-related to the FIB method, both methods can also be used in the steady Stokes limit [20]. At the level of the mathematical (continuum) formulation the SELM, fluctuating FCM and FIB methods are very similar, though the numerical techniques used to discretize and solve the equations of motion are rather distinct, leading to several crucial differences between the work presented here and existing work. Specifically, we develop novel temporal integrators that efficiently account for the dependence of the mobility on configuration, which is crucial in confined geometries. Crucially, we do not assume specific forms of the boundary conditions when solving the fluid (steady or unsteady) Stokes equations, and, in particular, we do not rely on periodic boundary conditions and using a Fourier basis (and the associated FFTs) to diagonalize the Stokes operator [20, 50]. Furthermore, we do not use Gaussian kernels as in the FCM, rather, we employ the compact-support kernels Peskin specifically constructed for immersed-boundary discretizations that employ a finite-difference-type discretization of the fluid equations [54]. Note also that we handle domain boundaries (for both deterministic *and* stochastic terms) directly in the finite-volume fluctuating Stokes solver, unlike recent extensions to BD [29] that handle complex boundaries by discretizing the boundary using immersed-boundary techniques. Independently of our work, an extension to SELM to nonperiodic domains, but using a finite-element rather than a finite-volume Stokes solver, has recently been developed [55]. We will defer a more detailed comparison with this related but distinct work until the concluding section, after we present the technical details of the FIB method.

This paper is organized as follows. In the remainder of this section we summarize the well-known and widely-used method of Brownian dynamics, to the extent necessary for subsequent comparison with our FIB method. In Section II we discuss the equations of motion solved in the FIB method at the continuum level, and explain the relation to the equations of Brownian dynamics. Then, we explain how we discretize those equations in both space (Section III) and time (Section IV). In Section V we perform a series of validation tests confirming the accuracy and robustness of the FIB method on a variety of tests of increasing complexity. Several technical derivations are detailed in the Appendix.

## A. Brownian Dynamics

The equations of Brownian Dynamics (BD) model the diffusive dynamics of the positions  $\mathbf{q}(t) = \{\mathbf{q}_1(t), \dots, \mathbf{q}_N(t)\}$  of a collection of  $N$  particles via the Ito system of stochastic differential equations,

$$\frac{d\mathbf{q}}{dt} = \mathbf{M}\mathbf{F} + \sqrt{2k_B T} \mathbf{M}^{\frac{1}{2}} \widetilde{\mathbf{W}}(t) + k_B T (\partial_{\mathbf{q}} \cdot \mathbf{M}), \quad (1)$$

where  $\mathbf{M}(\mathbf{q}) \succeq \mathbf{0}$  is the symmetric positive semidefinite (SPD) mobility matrix, relating the applied forces,  $\mathbf{F}(\mathbf{q}) = -\partial U(\mathbf{q})/\partial \mathbf{q}$  with  $U(\mathbf{q})$  a conservative potential, to the resulting (deterministic) velocity. For notational brevity we will often omit the explicit dependence on the configuration  $\mathbf{q}$  or time  $t$ . The stochastic forcing  $\widetilde{\mathbf{W}}(t)$  denotes a vector of independent white noise process, formally time derivatives of independent Wiener processes. The “square root” of the mobility  $\mathbf{M}^{\frac{1}{2}}$  is a matrix (not necessarily square) which satisfies the fluctuation dissipation balance condition

$$\mathbf{M}^{\frac{1}{2}} (\mathbf{M}^{\frac{1}{2}})^* = \mathbf{M}. \quad (2)$$

We use a superscript star throughout to denote the adjoint of a linear operator for a suitably-weighted inner product (conjugate transpose for matrices for the standard inner product). Throughout this paper we will rewrite the equations of motion (1) to eliminate the final “thermal”, “stochastic” or “spurious” drift term  $k_B T (\partial_{\mathbf{q}} \cdot \mathbf{M})$  by using the *kinetic* interpretation of the stochastic integral [56], denoted in this paper by the stochastic product symbol  $\diamond$ ,

$$\frac{d\mathbf{q}(t)}{dt} = \mathbf{M}(\mathbf{q})\mathbf{F}(\mathbf{q}) + \sqrt{2k_B T} \mathbf{M}^{\frac{1}{2}}(\mathbf{q}) \diamond \widetilde{\mathbf{W}}(t). \quad (3)$$

Condition (2) insures that the dynamics (3) is time-reversible with respect to the Gibbs-Boltzmann distribution

$$P_{eq}(\mathbf{q}) = Z^{-1} \exp(-U(\mathbf{q})/k_B T), \quad (4)$$

where  $Z$  is a normalization constant. This may be seen by examining the Fokker-Planck equation for the evolution of the probability distribution for observing the state  $\mathbf{q}$  at time  $t$  corresponding to (1) or (3),

$$\frac{\partial P}{\partial t} = \frac{\partial}{\partial \mathbf{q}} \cdot \left\{ \mathbf{M} \left[ \frac{\partial U}{\partial \mathbf{q}} P + (k_B T) \frac{\partial P}{\partial \mathbf{q}} \right] \right\}, \quad (5)$$

and noting that the term in square brackets vanishes when  $P = P_{eq}$ .

Developing schemes to simulate Brownian dynamics has several challenges. One such challenge is evaluating, or more precisely, applying the mobility matrix, which contains all of the information about hydrodynamic interactions between the particles. This can be non-trivial to achieve analytically even in relatively simple geometries,

and the mobility is generally approximated via a multipole expansion or infinite series of images. Special care must be taken to insure that the truncation of these infinite series result in a positive-semidefinite matrix [32, 37]. Even if an efficient application of the action of the mobility matrix is available, one still must also be able to generate the action of  $\mathbf{M}^{\frac{1}{2}}$ , typically approximated by Chebyshev polynomials as originally proposed by Fixman [57]. Finally, the thermal drift term  $k_B T \partial_{\mathbf{q}} \cdot (\mathbf{M}(\mathbf{q}))$  must be calculated or approximated in some way. This amounts to consistently discretizing the kinetic interpretation of the stochastic integral, which is traditionally accomplished by using the Fixman midpoint algorithm [56]. Note however that the Fixman method (and in general the use of the kinetic stochastic integral) requires handling the inverse of the mobility matrix, which can add substantial complication and cost [20].

## B. Mobility Matrix

For two well-separated spherical particles  $i$  and  $j$ , we can approximate the pairwise mobility, which determines the velocity on particle  $i$  resulting from a force on particle  $j$ , with [15, 32]

$$\mathbf{M}_{ij} = \mathbf{M}_{ji} = \eta^{-1} \left( \mathbf{I} + \frac{a^2}{6} \nabla_{\mathbf{r}}^2 \right) \left( \mathbf{I} + \frac{a^2}{6} \nabla_{\mathbf{r}'}^2 \right) \mathbf{K}(\mathbf{r}, \mathbf{r}')|_{\mathbf{r}'=\mathbf{q}_i}^{\mathbf{r}=\mathbf{q}_j}, \quad (6)$$

where  $a$  is the radius of the particles. Here  $\mathbf{K}$  is the Green’s function for the steady Stokes problem with unit viscosity, with the appropriate boundary conditions such as no-slip on the boundaries of the domain. The differential operator  $\mathbf{I} + (a^2/6) \nabla^2$  is called the Faxen operator [15] and leads to the well-known Faxen correction to the Stokes drag law. Note that the form of (6) guarantees that an SPD mobility matrix is obtained by construction.

### 1. Unconfined systems

For a three dimensional unbounded domain with fluid at rest at infinity,  $\mathbf{K}(\mathbf{r}, \mathbf{r}') = \mathbf{K}(\mathbf{r} - \mathbf{r}')$  is isotropic and given by the Oseen tensor,

$$\mathbf{K}(\mathbf{r}) = \mathbf{O}(\mathbf{r}) = \frac{1}{8\pi r} \left( \mathbf{I} + \frac{\mathbf{r} \otimes \mathbf{r}}{r^2} \right).$$

For many particles in an unbounded domain, applying (6) to the Oseen tensor yields the far-field expression of the Rotne-Prager-Yamakawa (RPY) tensor [58], commonly used in Brownian dynamics simulations. A correction needs to be introduced when particles are close to each other in order to produce a mobility which is positive

definite [58],

$$\mathcal{M}_{ij} = \frac{1}{6\pi\eta a} \begin{cases} C_1(r_{ij})\mathbf{I} + C_2(r_{ij})\frac{\mathbf{r}_{ij}\otimes\mathbf{r}_{ij}}{r_{ij}^2}, & r_{ij} > 2a \\ C_3(r_{ij})\mathbf{I} + C_4(r_{ij})\frac{\mathbf{r}_{ij}\otimes\mathbf{r}_{ij}}{r_{ij}^2}, & r_{ij} \leq 2a \end{cases} \quad (7)$$

where  $\mathbf{r}_{ij} = \mathbf{q}_i - \mathbf{q}_j$  is the vector connecting the particles, and  $r_{ij}$  is its length, and

$$\begin{aligned} C_1(r_{ij}) &= \frac{3a}{4r_{ij}} + \frac{a^3}{2r_{ij}^3} & C_2(r_{ij}) &= \frac{3a}{4r_{ij}} - \frac{3a^3}{2r_{ij}^3} \\ C_3(r_{ij}) &= 1 - \frac{9r_{ij}}{32a} & C_4(r_{ij}) &= \frac{3r_{ij}}{32a}. \end{aligned}$$

The diagonal blocks of the mobility matrix, i.e., the self-mobility can be obtained by setting  $r_{ij} = 0$  (giving  $C_3(0) = 1$  and  $C_4(0) = 0$ ) to obtain  $\mathcal{M}_{ii} = (6\pi\eta a)^{-1}\mathbf{I}$ , which matches the Stokes solution for the drag for flow around a sphere. It is important physically that  $\mathcal{M}_{ij} = \mathcal{M}_{ii}$  when  $r_{ij} = 0$  since two perfectly overlapping particles must behave as if there is only a single particle at that location.

For a single particle in an unbounded domain it is obvious that  $\mathcal{M}_{ii}$  is constant and thus has vanishing divergence. For the RPY mobility it can be shown that  $\partial_{\mathbf{q}} \cdot (\mathcal{M}(\mathbf{q})) = \mathbf{0}$  even for multi-particle systems (this is in fact a rather generic consequence of the incompressibility of the flow [59]). Note, however, that when stresslet terms are included the mobility becomes a complicated function of configuration (see Appendix B) and the stochastic drift term must be accounted for [20].

## 2. Confined systems

In the presence of boundaries, the Green's function may be decomposed as

$$\mathbf{K}(\mathbf{r}, \mathbf{r}') = \mathbf{O}(\mathbf{r} - \mathbf{r}') + \mathbf{K}^w(\mathbf{r}, \mathbf{r}'), \quad (8)$$

where  $\mathbf{K}^w$  is the Green's function for a disturbance velocity field enforcing the no-slip condition at the walls. One can approximate the pairwise far-field mobility by using (6) and applying the Faxen operators to  $\mathbf{O}$  and  $\mathbf{K}^w$  separately [32]. For the diagonal blocks, we have to consider the self-mobility in an unbounded domain separately, and only use (6) with  $\mathbf{K}$  replaced by  $\mathbf{K}^w$  in order to account for the disturbance velocity from the boundary conditions [32] (equivalently, to account for the hydrodynamic interactions with the image particles),

$$\begin{aligned} \mathcal{M}_{ii} &= \frac{1}{6\pi\eta a}\mathbf{I} \\ &+ \eta^{-1} \left( \mathbf{I} + \frac{a^2}{6}\nabla_{\mathbf{r}}^2 \right) \left( \mathbf{I} + \frac{a^2}{6}\nabla_{\mathbf{r}'}^2 \right) \mathbf{K}^w(\mathbf{r}, \mathbf{r}')|_{\mathbf{r}=\mathbf{q}_i}^{\mathbf{r}'=\mathbf{q}_i}. \end{aligned}$$

Note that this approach requires knowing the Green's function for the particular geometry in question. For a single no-slip wall  $\mathbf{K}^w$  was obtained by Blake [60], but

for a slit channel with two no-slip walls there is no manageable analytical form [37].

It is important to note that even for a single particle near a boundary the mobility strongly depends on the position of the particle relative to the boundary and therefore the thermal drift  $k_B T \partial_{\mathbf{q}} \cdot \mathcal{M}$  must be accounted for [37].

## II. FLUCTUATING IMMERSED BOUNDARY METHOD

In this section we present the continuum formulation of the equations of motion as employed in the FIB method. At the same time, we use operator notation that generalizes to spatially-discretized equations, by simply replacing the continuum integro-differential operators with sums and differences (matrices), see the discussion of Atzberger [17] for more details. This makes the majority of this section directly transferable to the semi-discrete setting presented in Section III. The operator notation we employ also enables us to treat in a unified way different boundary conditions without requiring a specific basis for the solution of the Stokes equations.

We consider  $n$  spherical neutrally-buoyant particles of radius  $a$  in  $d$  dimensions, having spatial positions  $\mathbf{q} = \{\mathbf{q}_1, \dots, \mathbf{q}_N\}$  with  $\mathbf{q}_i = (q_i^{(1)}, \dots, q_n^{(d)})$ . These particles are immersed in an incompressible fluid of constant density  $\rho$ , temperature  $T$ , and viscosity  $\eta$ , and described by the fluctuating time dependent Stokes equations for the fluid velocity  $\mathbf{v}(\mathbf{r}, t)$ ,

$$\begin{aligned} \rho \partial_t \mathbf{v} + \nabla \pi &= \eta \nabla^2 \mathbf{v} + \mathbf{f} + \sqrt{2\eta k_B T} \nabla \cdot \mathcal{Z} \\ \nabla \cdot \mathbf{v} &= 0, \end{aligned} \quad (9)$$

along with appropriate boundary conditions. Here  $\mathbf{f}(\mathbf{r}, t)$  is a force density applied to the fluid,  $k_B$  is Boltzmann's constant, and  $\mathcal{Z}(\mathbf{r}, t)$  is a random Gaussian tensor field whose components are white in space and time with mean zero [5],

$$\langle \mathcal{Z}_{ij}(\mathbf{r}, t) \mathcal{Z}_{kl}(\mathbf{r}', t') \rangle = (\delta_{ik} \delta_{jl} + \delta_{il} \delta_{jk}) \delta(t - t') \delta(\mathbf{r} - \mathbf{r}'). \quad (10)$$

The coupling between the fluid and particles employed here is used in a large number of other methods and related prior work. In particular, the same basic equations are employed in SIBM [50, 61] and SELM [17]. In the deterministic setting, Maxey and collaborators have developed in extensive detail the use of smooth envelope or kernel function to represent particles in flow in the context of the Force Coupling Method (FCM) [51, 52, 62]. Recently, Keaveny has included fluctuations in the description in a manner fully consistent with our presentation [20]. Similar representations of particles have also been used with the Lattice Boltzmann method [16, 63]. Both Atzberger [61] and Keaveny [20] have already noted the relation to Brownian and Stokesian dynamics. Nevertheless, for completeness and clarity and the benefit of

the reader, here we present a unified view of these somewhat disjoint works and point out some less-appreciated but important features.

### A. Fluid-Particle Interaction

In the FIB method, the shape of the particle and its effective interaction with the fluid is captured through a smooth kernel function  $\delta_a(\mathbf{r})$  that integrates to unity and whose support is localized in a region of size  $a$ . This kernel is used to mediate two crucial operations. First, it is used to transfer (spread) the force exerted on the particle to the fluid. Second, it is used to impose a minimally-resolved form of the no-slip constraint stating that the velocity of the particle equals the local velocity of the fluid. Following Refs. [19, 21, 64, 65] we term this diffuse (rather than “point”) particle a *blob* for lack of better terminology (in polymer modeling the term bead is used for the same concept [16]).

In order to couple the fluid velocity field to the motion of immersed particles, we introduce composite local averaging  $\mathcal{J}(\mathbf{q})$  and spreading  $\mathcal{S}(\mathbf{q})$  operators. The operator  $\mathcal{J}(\mathbf{q})$  takes a continuous velocity field  $\mathbf{v}(\mathbf{r})$  and computes its local average at the position of each particle, while  $\mathcal{S}(\mathbf{q})$  takes the forces  $\mathbf{F} = \{\mathbf{F}_1, \dots, \mathbf{F}_N\}$  applied on the particles and computes a smooth force density field,

$$(\mathcal{J}(\mathbf{q})\mathbf{v}(\mathbf{r}))_i = \int \delta_a(\mathbf{q}_i - \mathbf{r})\mathbf{v}(\mathbf{r})d\mathbf{r} \quad (11)$$

$$(\mathcal{S}(\mathbf{q})\mathbf{F})(\mathbf{r}) = \sum_i \delta_a(\mathbf{q}_i - \mathbf{r})\mathbf{F}_i. \quad (12)$$

Note that  $\mathcal{J}$  is dimensionless, and  $\mathcal{S}$  has units of inverse volume. The blobs are assumed to move with the locally-averaged fluid velocity,

$$\frac{d\mathbf{q}(t)}{dt} = \mathcal{J}(\mathbf{q})\mathbf{v}(\mathbf{r}, t), \quad (13)$$

which is a minimally-resolved representation of the *no-slip constraint* [19, 64]. Furthermore, the applied forces  $\mathbf{F}$  affect the motion of the fluid through the addition of a continuous force density to the fluid equation (9),

$$\mathbf{f} = \mathcal{S}(\mathbf{q})\mathbf{F} + \mathbf{f}_{\text{th}}, \quad (14)$$

where  $\mathbf{f}_{\text{th}}$  is a thermal or stochastic forcing that we discuss shortly. It is crucial for energy conservation and fluctuation-dissipation balance that the coupling operators are adjoints of one another [17, 19, 52],  $\mathcal{J} = \mathcal{S}^*$ , as follows from

$$\sum_i (\mathcal{J}\mathbf{v})_i \cdot \mathbf{u}_i = \int \mathbf{v} \cdot (\mathcal{S}\mathbf{u}) d\mathbf{r} = \int \sum_i \delta_a(\mathbf{q}_i - \mathbf{r}) (\mathbf{v} \cdot \mathbf{u}_i) d\mathbf{r} \quad (15)$$

In this work we focus on suspensions of spherical particles (blobs), for which the kernel function  $\delta_a(\mathbf{r}) \equiv \delta_a(r)$

should be taken to be a spherically-symmetric function of width  $\sim a$ . In our computational algorithm we employ the compact-support kernels of Peskin [54], which are of the tensor product form  $\delta_a(\mathbf{r}) = \prod_{\alpha=1}^d \delta_a(r_\alpha)$  and are specifically designed to work well in the discrete context, as discussed further in Section III. Note that a Gaussian kernel, as used in FCM [51, 52], has the special property that it is of the tensor product form while also being isotropic. It should be noted, however, that much more general forms of the local interpolation and spreading operators are possible [17]; this has been successfully used to generalize FCM to non-spherical particles [53] and can also be used to further extend our FIB method. The local averaging and spreading operators have to be modified near physical boundaries, specifically, when the support of the kernel  $\delta_a$  overlaps with a boundary. A proposal for how to do that has been developed by Yeo and Maxey [62], and we have found it to be superior to an alternative proposal developed in the context of the immersed boundary method in Ref. [66]. In practice a repulsive potential is imposed between the boundaries and the particles, which may be sufficient to keep the kernels from overlapping the walls.

In order to ensure that the system of equations (9,13,14) obeys fluctuation-dissipation (i.e., that the dynamics is time reversible with respect to an appropriate Gibbs-Boltzmann distribution), the thermal forcing

$$\mathbf{f}_{\text{th}} = (k_B T) \partial_{\mathbf{q}} \cdot \mathcal{S} \quad (16)$$

should be included in the fluid equations, as derived by Atzberger [17] and also discussed from a different perspective in Appendix B in Ref. [19] and Ref. [21]. Here we use the convention that the contraction in the divergence of an operator is on the second index,  $f_i^{\text{th}} = k_B T \partial_j \mathcal{S}_{ij}$ , consistent with Ref. [17] but not with Ref. [19]; to avoid confusion we will write things out in indicial notation when necessary [99]. For a translationally-invariant (e.g., periodic) system and kernel, this term can be omitted. Namely, from the definition (12) it follows that  $\mathbf{f}_{\text{th}} = -(k_B T) \nabla_{\mathbf{r}} \cdot \sum_i \delta(\mathbf{q}_i - \mathbf{r})$ , and the solution of the incompressible velocity equations is not affected by the addition of a gradient of a scalar. This is not strictly true in the discrete setting (see Section V C 1) and may not generalize to confined (i.e., not translationally-invariant) systems for particles in the vicinity of boundaries. The term (16) is therefore, in general, required in order to obtain discrete fluctuation-dissipation balance and is included in our temporal integrator.

### B. Overdamped Limit

Equations (9), (13), and (14) together constitute a physically-realistic description which obeys fluctuation-dissipation balance [17], including in the presence of additional particle inertia [19, 67]. Here we are interested in the inertia-less or overdamped limit, where the momentum of the fluid may be eliminated as a fast variable.

More precisely, we assume that the Schmidt number is very large,  $Sc = \eta / (\rho\chi) \gg 1$ , where  $\chi \approx k_B T / (6\pi\eta a)$  is a typical value of the diffusion coefficient of the particles [45].

Following the notation developed in [68], here we use  $\mathcal{Z}(\mathbf{r}, t)$  to denote an infinite-dimensional standard white-noise field, use  $\mathcal{W}(t)$  to denote a finite dimensional collection of standard white noise processes that represents a spatial discretization of  $\mathcal{Z}(\mathbf{r}, t)$ , and use  $\mathbf{W}$  to denote a collection of standard (mean zero and unit variance) Gaussian variates that appears when  $\mathcal{W}(t)$  is discretized in time. For notational clarity, and to emphasize that we also consider spatially-discretized operators in the following calculations, we introduce symbols for the various differential operators:  $\mathbf{D}$  for the divergence,  $\mathbf{G} = -\mathbf{D}^*$  for the gradient,  $\mathbf{L}$  for the vector Laplacian, and  $\tilde{\mathbf{D}}$  for the divergence operator acting on the stochastic tensor. In the infinite-dimensional (continuum) setting these are differential operators, while in the finite dimensional (discrete) setting they are matrices that approximate the corresponding differential operators (for example, using finite differences), taking into account the boundary conditions [69]. Note that the operator  $\tilde{\mathbf{D}}$  does not have to be a consistent representation of the tensor divergence, rather, all that matters is that the covariance of the stochastic fluid forcing  $\tilde{\mathbf{D}}\mathcal{W}$  obey the fluctuation-dissipation property  $\mathbf{L} = -\tilde{\mathbf{D}}\langle\mathcal{W}\mathcal{W}^*\rangle\tilde{\mathbf{D}}^*$  [55, 69]. For notational simplicity, here we assume that the components of  $\mathcal{W}$  are independent,  $\langle\mathcal{W}\mathcal{W}^*\rangle = \mathbf{I}$ , with the understanding that some modifications of either the covariance of  $\mathcal{W}$ , or, equivalently, the operator  $\tilde{\mathbf{D}}$ , may be necessary near boundaries to preserve fluctuation-dissipation balance for confined systems [69].

To obtain the asymptotic dynamics in the limit  $Sc \rightarrow \infty$  heuristically, we delete the inertial term  $\rho\partial_t \mathbf{v}$  in (9) to obtain the (potentially discretized) fluctuating steady Stokes equations for the velocity  $\mathbf{v}$  and the pressure  $\pi$ ,

$$\begin{aligned} \mathbf{G}\pi - \eta\mathbf{L}\mathbf{v} &= \mathbf{g} + \mathcal{S}\mathbf{F} + \sqrt{2k_B T\eta}\tilde{\mathbf{D}}\mathcal{W} \\ \mathbf{D}\mathbf{v} &= 0, \end{aligned} \quad (17)$$

with appropriate boundary conditions. For periodic systems we additionally constrain the average velocity  $\langle\mathbf{v}\rangle = 0$  to eliminate the non-trivial nullspace. In the following we will denote with  $\mathcal{L}^{-1}$  the (continuum or discrete) Stokes solution operator for the system (17) with unit viscosity,  $\mathbf{v} = \eta^{-1}\mathcal{L}^{-1}\mathbf{g}$ . Note that  $\mathcal{L}^{-1} \succeq 0$  is SPD because the Stokes problem (17) is symmetric by virtue of the adjoint relation  $\mathbf{G} = -\mathbf{D}^*$  and the Laplacian operator  $\mathbf{L}$  is symmetric negative semi-definite.

In the overdamped regime, the (fast) fluid velocity evolves instantaneously to its steady state and may be viewed as a random function of the particles' positions, which are the relevant (slow) variables. Heuristically, one expects that the Brownian dynamics of the particles is described by  $d\mathbf{q}/dt = \mathbf{v} = \eta^{-1}\mathcal{L}^{-1}\mathbf{g}$ . A rigorous adiabatic mode elimination procedure [70, 71] informs us that the correct interpretation of the noise term in this

equation is the kinetic one, leading to the overdamped Langevin equation

$$\frac{d\mathbf{q}(t)}{dt} = \mathcal{J}(\mathbf{q})\mathcal{L}^{-1} \left[ \frac{1}{\eta}\mathcal{S}(\mathbf{q})\mathbf{F}(\mathbf{q}) + \sqrt{\frac{2k_B T}{\eta}}\tilde{\mathbf{D}} \diamond \mathcal{W}(t) \right]. \quad (18)$$

This is the rigorous asymptotic limit of (9,13,14) as  $Sc \rightarrow \infty$  [72] and it is the equation of motion in the FIB method.

### C. Relation to Brownian Dynamics

A key observation is that (18) is a specific instance of the equation of Brownian dynamics (3), with the identification

$$\mathcal{M} = \eta^{-1}\mathcal{J}\mathcal{L}^{-1}\mathcal{S} \quad \text{and} \quad \mathcal{M}^{\frac{1}{2}} = \eta^{-\frac{1}{2}}\mathcal{J}\mathcal{L}^{-1}\tilde{\mathbf{D}}. \quad (19)$$

To demonstrate that this choice satisfies the fluctuation dissipation balance condition (2), note the adjoint relations  $\mathcal{J} = \mathcal{S}^*$  and  $\mathbf{L} = -\tilde{\mathbf{D}}\tilde{\mathbf{D}}^*$ . It is important to point out that the spatially-discretized operators we employ obey these properties even in the presence of nontrivial boundary conditions [69]. Observe also that

$$-\mathcal{L}^{-1}\mathbf{L}\mathcal{L}^{-1} = \mathcal{L}^{-1} \quad (20)$$

as seen from their action on an arbitrary vector  $\mathbf{g}$ ,

$$\begin{aligned} -\mathcal{L}^{-1}\mathbf{L}\mathcal{L}^{-1}\mathbf{g} &= -\mathcal{L}^{-1}\eta\mathbf{L}\mathbf{v} = \\ \mathcal{L}^{-1}(-\mathbf{G}\pi + \mathbf{g}) &= \mathcal{L}^{-1}\mathbf{g}, \end{aligned}$$

where we used the fact that  $\mathcal{L}^{-1}\mathbf{G} = 0$  since adding a gradient forcing to the Stokes equations does not affect the velocity. This gives

$$\begin{aligned} \mathcal{M}^{\frac{1}{2}}\left(\mathcal{M}^{\frac{1}{2}}\right)^* &= \eta^{-1}\mathcal{J}\mathcal{L}^{-1}\left(\tilde{\mathbf{D}}\tilde{\mathbf{D}}^*\right)\mathcal{L}^{-1}\mathcal{S} = \\ -\eta^{-1}\mathcal{J}\left(\mathcal{L}^{-1}\mathbf{L}\mathcal{L}^{-1}\right)\mathcal{S} &= \eta^{-1}\mathcal{J}\mathcal{L}^{-1}\mathcal{S} = \mathcal{M}. \end{aligned} \quad (21)$$

Also note that the mobility (19) is guaranteed to be positive-semidefinite by virtue of (2).

More explicitly, (19) gives a pairwise mobility [100] that only depends on the position of the pair of particles under consideration [61],

$$\mathcal{M}_{ij} = \eta^{-1} \int \delta_a(\mathbf{q}_i - \mathbf{r})\mathbf{K}(\mathbf{r}, \mathbf{r}')\delta_a(\mathbf{q}_j - \mathbf{r}') d\mathbf{r}d\mathbf{r}' \quad (22)$$

where we recall that  $\mathbf{K}$  is the Green's function for the Stokes problem with unit viscosity and the specified boundary conditions. Note that in our approach the self-mobility  $\mathcal{M}_{ii}$  is also given by the same formula (22) with  $i = j$  and does not need to be treated separately. In fact, the self-mobility of a particle in an unbounded three-dimensional domain defines the effective hydrodynamic radius  $a$  of a blob,

$$\begin{aligned} \mathcal{M}_{ii} &= \mathcal{M}_{\text{self}} = \frac{1}{6\pi\eta a}\mathbf{I} = \\ \eta^{-1} \int \delta_a(\mathbf{q}_i - \mathbf{r})\mathbf{O}(\mathbf{r} - \mathbf{r}')\delta_a(\mathbf{q}_i - \mathbf{r}') d\mathbf{r}d\mathbf{r}'. \end{aligned}$$

The value of  $a$  will therefore depend on the specific kernel used, as discussed further in section III A. In two dimensions, the self-mobility  $\mathcal{M}_{\text{self}} = \mu \mathbf{I}$  of a disk of radius  $a$  in a periodic domain (equivalently, a periodic array of infinite cylinders) grows logarithmically with the length of the square periodic cell  $L$  as  $\mu = (4\pi\eta)^{-1} \ln(L/3.708a)$  [73]. The same scaling with the system size holds for a blob and can be used to define an effective hydrodynamic radius for a two-dimensional blob [45]. Note that in two dimensions the mobility diverges for an infinite domain, in agreement with Stokes's paradox.

Maxey [52] observed that (22) consistently includes the Faxen correction to the mobility of two well-separated particles. Let  $\mathbf{J}(\mathbf{q}_i)$  denote the local averaging operator for a particle  $i$ ,  $\mathbf{J}(\mathbf{q}_i) \mathbf{v} \equiv (\mathcal{J}(\mathbf{q}) \mathbf{v})_i$ . For a smooth velocity field, we can perform a second order Taylor expansion of the velocity field,

$$\begin{aligned} \mathbf{J}(\mathbf{q}_i) \mathbf{v}(\mathbf{r}) &= \int \delta_a(\mathbf{q}_i - \mathbf{r}) \mathbf{v}(\mathbf{r}) d\mathbf{r} \\ &\approx \left[ \mathbf{I} + \left( \int \frac{x^2}{2} \delta_a(x) dx \right) \nabla^2 \right] \mathbf{v}(\mathbf{r})|_{\mathbf{r}=\mathbf{q}_i} \\ &= \left( \mathbf{I} + \frac{a_F^2}{6} \nabla^2 \right) \mathbf{v}(\mathbf{r})|_{\mathbf{r}=\mathbf{q}_i}, \end{aligned}$$

where we assumed a spherical blob,  $\delta_a(\mathbf{r}) \equiv \delta_a(r)$ . This shows that we can approximate the local averaging operator by a differential operator that is identical in form to the Faxen operator appearing in (6), if we define the ‘‘Faxen’’ radius of the blob  $a_F \equiv (3 \int x^2 \delta_a(x) dx)^{1/2}$  through the second moment of the kernel function. In general,  $a_F \neq a$ , but for a suitable choice of the kernel one can accomplish  $a_F \approx a$  and thus accurately obtain the Faxen correction for a rigid sphere (for example, for a Gaussian  $a/a_F = \sqrt{3/\pi}$  [52]). Interestingly, it has been shown that the leading-order Faxen corrections to the linear and angular velocities of an ellipsoidal particle can also be captured remarkably accurately (to within 5%) by using a stretched and rotated Gaussian for the kernel function [53].

The calculations above show that the mobility tensor for a pair of blobs (22) is a good approximation to (6) for well-separated blobs and thus correctly captures the mobility up to the Rotne-Prager level even in the presence of confinement. This can also be seen from (22) by noting that when the two particles are well separated,  $\mathbf{K}$  is a smooth function, and is well approximated by a Taylor series, giving

$$\mathcal{M}_{ij} \approx \eta^{-1} \left( \mathbf{I} + \frac{a_F^2}{6} \nabla_{\mathbf{r}}^2 \right) \left( \mathbf{I} + \frac{a_F^2}{6} \nabla_{\mathbf{r}'}^2 \right) \mathbf{K}(\mathbf{r}-\mathbf{r}')|_{\mathbf{r}'=\mathbf{q}_i}^{\mathbf{r}=\mathbf{q}_j},$$

which matches the expression (6) for well-separated rigid spheres. At smaller distances the mobility is mollified (regularized) in a natural way without requiring any special handling of the case  $r_{ij} < 2a$  as in the traditional RPY tensor (7). Furthermore, a positive definite mobility tensor is obtained by construction. Most importantly,

the same continues to hold in the presence of confinement (nontrivial boundary conditions). The boundary conditions are taken into account by the fluid solver when computing the action of the Green's function (8), while the regularization and the Faxen corrections are handled via the local averaging and spreading operators. This inherent self-consistency of the formulation is inherited from the underlying fluctuating hydrodynamics formulation (9,13,14) [19].

## D. Thermal Drift

One key difference between the inertial formulation (9,13,14) and the overdamped limit (18) is the fact that the noise in (18) is multiplicative and therefore the stochastic interpretation matters and affects the temporal discretization. Methods for integrating (3) have been developed in the Brownian Dynamics literature, however, here we propose a more efficient approach which we term Random Finite Difference (RFD). We believe this approach will find uses in Brownian Dynamics simulations as well as related methods for fluctuating hydrodynamics [20, 55]. We therefore explain it here in the more general setting of solving (3), of which (18) is a special instance. A detailed description of predictor-corrector schemes to solve (18) is given in Section IV.

Of course, one can use the Ito equation (1) with integrators based on the Euler-Maruyama scheme. This, however, requires computing the stochastic drift term  $k_B T (\partial_{\mathbf{q}} \cdot \mathcal{M})$ , which is difficult in general. First, we summarize the well-known Fixman midpoint approach to approximating  $\partial_{\mathbf{q}} \cdot \mathcal{M}(\mathbf{q})$ , and use it to construct an RFD approach that works better in the context of our explicit fluid method. Below we use the superscript to denote the time step level at which quantities are evaluated, for example,  $\mathcal{M}^n \equiv \mathcal{M}(\mathbf{q}^n)$  denotes the mobility evaluated at the beginning of time step  $n$ , while  $\mathcal{M}^{n+\frac{1}{2}} \equiv \mathcal{M}(\mathbf{q}^{n+\frac{1}{2}})$  denotes a midpoint approximation of the mobility during time step  $n$ .

### 1. Fixman's Method

The Fixman midpoint scheme used to capture the thermal drift [24, 25] can be seen as corresponding to a direct discretization of the kinetic stochastic integral [56],

$$\begin{aligned} \mathbf{q}^{n+\frac{1}{2}} &= \mathbf{q}^n + \frac{\Delta t}{2} \mathcal{M}^n \mathbf{F}^n \\ &\quad + \sqrt{\frac{\Delta t k_B T}{2}} (\mathcal{M}^n)^{\frac{1}{2}} \mathbf{W}^n \\ \mathbf{q}^{n+1} &= \mathbf{q}^n + \Delta t \mathcal{M}^{n+\frac{1}{2}} \mathbf{F}^{n+\frac{1}{2}} \\ &\quad + \sqrt{2\Delta t k_B T} \mathcal{M}^{n+\frac{1}{2}} (\mathcal{M}^n)^{-\frac{1}{2}} \mathbf{W}^n, \quad (23) \end{aligned}$$

where  $\mathbf{W}^n$  is a vector of i.i.d. standard Gaussian variables and

$$(\mathcal{M}^n)^{-\frac{1}{2}} \left( (\mathcal{M}^n)^{-\frac{1}{2}} \right)^* = (\mathcal{M}^n)^{-1}.$$

While the Fixman method is quite elegant and has been widely used with notable success, it requires handling the inverse of the mobility matrix, which would add significant complication to our method [20].

In order to show that (23) is consistent with (3) one has to show that the first and second moments of the increment  $\mathbf{q}^{n+1} - \mathbf{q}^n$  are  $O(\Delta t)$  with coefficients matching the drift and diffusion terms in the Ito equation (18), and higher moments should be of higher order in  $\Delta t$ . The only nontrivial component is the stochastic drift term  $k_B T \partial_{\mathbf{q}} \cdot \mathcal{M}(\mathbf{q})$ . In order to compact the notation, henceforth we will index matrices and vectors without regard for the physical particles represented. For example, we will write  $q_i$  to represent the scalar that is the  $i$ th entry of the length  $nd$  vector of positions  $\mathbf{q}$ , disregarding which particle this entry describes. We will likewise consider the mobility  $\mathcal{M}$  as a matrix of scalars  $\mathcal{M}_{ij}$ . This allows us to use Einstein summation notation and indicial algebra. We can show that the Fixman algorithm (23) generates the correct stochastic drift term from

$$\lim_{\Delta t \rightarrow 0} \frac{1}{\Delta t} \left\langle \mathcal{M}_{ij} \left( q_p^n + \sqrt{\frac{\Delta t k_B T}{2}} (\mathcal{M}_{pr}^n)^{\frac{1}{2}} W_r^n \right) \times \sqrt{2 \Delta t k_B T} (\mathcal{M}_{jk}^n)^{-\frac{1}{2}} W_k^n \right\rangle = k_B T \partial_j \mathcal{M}_{ij}(\mathbf{q}^n), \quad (24)$$

where the average is over realizations of  $\mathbf{W}$  and the shorthand  $\partial_j$  denotes a partial derivative with respect to the  $j$ -th component of  $\mathbf{q}$ .

## 2. Random Finite Difference

The equivalence (24) only relies on the covariance structure of  $\mathbf{W}^n$ , and there is no reason that we must use an increment that is related in any way to the noise term in (3). More generally, we can obtain a divergence of the mobility in expectation from the general relation,

$$\lim_{\epsilon \rightarrow 0} \frac{1}{\epsilon} \langle \mathcal{M}(\mathbf{q} + \epsilon \Delta \mathbf{q}) \Delta \mathbf{p} - \mathcal{M}(\mathbf{q}) \Delta \mathbf{p} \rangle = \partial_{\mathbf{q}} \cdot \mathcal{M}(\mathbf{q}), \quad (25)$$

where  $\Delta \mathbf{q}$  and  $\Delta \mathbf{p}$  are Gaussian variates with mean zero and covariance  $\langle \Delta q_i \Delta p_j \rangle = \delta_{ij}$ . In particular, the choice  $\Delta \mathbf{q} = \Delta \mathbf{p}$  is much simpler to use than the Fixman method choice  $\Delta \mathbf{q} \sim (\mathcal{M}^n)^{\frac{1}{2}} \mathbf{W}^n$  and  $\Delta \mathbf{p} \sim (\mathcal{M}^n)^{-\frac{1}{2}} \mathbf{W}^n$ . Here  $\epsilon$  is a small discretization parameter that can be taken to be related to  $\Delta t$  as in the Fixman method, but this is not necessary. One can more appropriately think of (25) as a “random finite difference” (RFD) with  $\epsilon$  representing the small spacing for the finite difference, to be taken as small as possible while avoiding numerical roundoff problems. The advantage of the

“random” over a traditional finite difference is that only a small number of evaluations of the mobility per time step is required. Note that the subtraction of  $\mathcal{M}(\mathbf{q}) \Delta \mathbf{p}$  in (25) is necessary in order to control the variance of the RFD estimate. One can use a centered difference to improve the truncation error and obtain the correct thermal drift via the RFD

$$\begin{aligned} & \frac{1}{\delta} \left\langle \left( \mathcal{M}_{ij} \left( q_k^n + \frac{\delta}{2} \widetilde{W}_k \right) \widetilde{W}_j - \mathcal{M}_{ij} \left( q_k^n - \frac{\delta}{2} \widetilde{W}_k \right) \widetilde{W}_j \right) \right\rangle \\ &= \partial_j \mathcal{M}_{ij}(\mathbf{q}^n) + O(\delta^2), \end{aligned} \quad (26)$$

where  $\widetilde{\mathbf{W}}$  is a vector of  $dn$  i.i.d. standard Gaussian random variables and  $\delta$  is a small parameter.

While expression (26) could be used to approximate the drift term and may be a useful alternative to the Fixman scheme in related methods such as the fluctuating FCM [20], using an RFD of the form (26) requires at least one more Stokes solve per time step in order to evaluate the action of  $\mathcal{M}(\mathbf{q} + \epsilon \Delta \mathbf{q})$ . It is, however, possible to avoid the second Stokes solve by splitting the divergence of the mobility into two pieces,

$$\eta \partial_{\mathbf{q}} \cdot \mathcal{M} = \partial_{\mathbf{q}} \cdot (\mathcal{J} \mathcal{L}^{-1} \mathcal{S}) = (\partial_{\mathbf{q}} \mathcal{J}) : (\mathcal{L}^{-1} \mathcal{S}) + \mathcal{J} \mathcal{L}^{-1} (\partial_{\mathbf{q}} \cdot \mathcal{S}),$$

where colon denotes a double contraction, see (32). We approximate the first term involving the gradient  $\partial_{\mathbf{q}} \mathcal{J}$  using a standard two-stage Runge-Kutta (predictor-corrector) approach, and use an RFD to approximate  $\partial_{\mathbf{q}} \cdot \mathcal{S}$ , as explained in detail in Section IV.

## III. SPATIAL DISCRETIZATION

In this section we describe our spatial discretization of (18), which is constructed from components described in extensive detail in prior work by some of us; here we only briefly summarize the key points. The finite-volume solver used here to solve the fluctuating Stokes equations in confined domains is taken from Ref. [69], while the discretization of the fluid-particle interaction operators is based on the immersed-boundary method [54] and is described in extensive detail in Ref. [19]. The key novel component here is the use of a steady Stokes fluid solver to generate a fluctuating velocity, as also done in Refs. [20, 23, 55] using different techniques.

We discretize the fluid equation (9) using a standard staggered “marker and cell” (MAC) grid with uniform mesh width  $h$  in a rectangular domain with an arbitrary combination of periodic, no-slip, or free-slip boundaries. The differential operators  $\mathbf{D}$ ,  $\mathbf{G}$ , and  $\mathbf{L}$  are discretized on the staggered grid using standard second order centered differences. The stochastic stress tensor  $\mathcal{Z}(\mathbf{r}, t)$  is discretized as  $\Delta V^{-\frac{1}{2}} \mathcal{W}(t)$ , where the additional factor of  $\Delta V^{-\frac{1}{2}}$  comes from the fact that  $\mathcal{Z}$  is white in space [68]. Adjustments to the stochastic increments are made near boundaries to preserve the fluctuation-dissipation relation  $-\tilde{\mathbf{D}} \tilde{\mathbf{D}}^T = \mathbf{L}$  (more precisely, to ensure that  $\mathbf{L} = -\tilde{\mathbf{D}} \langle \mathcal{W} \mathcal{W}^T \rangle \tilde{\mathbf{D}}^T$ ) [69].



### A. Discrete Local Averaging and Spreading

The discrete operator (matrix)  $\mathcal{J}$  averages velocities on the staggered mesh by discretizing the integral  $\int \delta_a(\mathbf{q}_i - \mathbf{r}) \mathbf{v}(\mathbf{r}) d\mathbf{r}$  using a simple quadrature

$$(\mathcal{J}\mathbf{v})_i^\alpha = \sum_k \delta_a(\mathbf{q}_i - \mathbf{r}_k^\alpha) v_k^\alpha \Delta V,$$

where the sum is taken over faces  $k$  of the grid, and  $\Delta V$  is the volume of a grid cell. Here  $\alpha$  indexes coordinate directions ( $x, y, z$ ) as a superscript,  $\mathbf{r}_k^\alpha$  is the center of the grid face  $k$  in the direction  $\alpha$ , and  $v_k^\alpha \equiv v^{(\alpha)}(\mathbf{r}_k)$  is the staggered velocity field. Likewise,  $\mathcal{S}$  spreads forces to the staggered grid, and its expression remains identical to (11), but is evaluated only at faces of the staggered grid normal to the component of force being spread,

$$(\mathcal{S}\mathbf{F})_k^\alpha = \sum_i F_i^\alpha \delta_a(\mathbf{q}_i - \mathbf{r}_k^\alpha),$$

where now the sum is over the particles. Near no-slip physical boundaries, the discrete delta function is modified following the image-monopole construction proposed by Yeo and Maxey, see (2.17) in Ref. [62]; this is found to be superior to the modification proposed in Ref. [66].

For a uniform grid, the matrices representing the discrete local averaging and spreading operators are scaled transposes of each other,  $\mathcal{J}^T = \Delta V \mathcal{S}$ . Note that these discrete operators are adjoints like their continuum counterparts,  $\mathcal{J} = \mathcal{S}^*$ , but in an inner product that includes an appropriate weighting [17] because the integral over the domain in (15) is replaced by a sum over grid points  $k$ ,

$$\begin{aligned} \sum_i (\mathcal{J}\mathbf{v})_i \cdot \mathbf{F}_i &= \sum_{k,\alpha} v_k^\alpha (\mathcal{S}\mathbf{F})_k^\alpha \Delta V \\ &= \sum_{i,k,\alpha} \delta_a(\mathbf{q}_i - \mathbf{r}_k^\alpha) v_k^\alpha F_i^\alpha \Delta V. \end{aligned} \quad (27)$$

Note that this adjoint relation is strictly preserved even in the presence of no-slip boundaries.

In the majority of the simulations we use the four-point kernel of Peskin [54] to discretize the kernel  $\delta_a$ , although in some cases we employ the three-point discrete kernel function of Roma and Peskin [64, 74]. The effective hydrodynamic radius  $a$  for a given discrete kernel function can be obtained from the self-mobility of a blob in a periodic domain. For large periodic domains in three dimensions we numerically estimate the effective hydrodynamic (rigid sphere) radius to be  $a = (0.91 \pm 0.01)h$  for the three-point kernel [19, 64], and  $a = (1.255 \pm 0.005)h$  for the four-point kernel [65]. In two dimensions, the effective (rigid disk) hydrodynamic radii are estimated to be  $a = (0.72 \pm 0.01)h$  for the three point and  $a = (1.04 \pm 0.005)h$  for the four point kernel [45]. Note that the spatial discretization we use is not perfectly translationally invariant and there is a small variation of  $a$

(quoted above as an error bar) as the particle moves relative to the underlying fixed fluid grid [19, 65]. By using the Peskin four-point kernel instead of the three-point discrete kernel function the translational invariance of the spatial discretization can be improved, however, at a potentially significant increase in computational cost, particularly in three dimensions.

It is important to note that, perhaps unexpectedly, these Peskin kernels give close agreement between the hydrodynamic and the Faxen radii of the blob. For example, in three dimensions, the three-point kernel gives  $a_F \approx 0.93h$  (this number is again not exactly constant due to the imperfect translational invariance), as compared to  $a \approx 0.91h$ . Using the four-point kernel gives an even better agreement, with  $a \approx a_F \approx 1.25h$ . In particular, it is important to choose a kernel with a nonzero second moment in order to capture the Faxen corrections in a physically-realistic manner; this eliminates the Peskin six-point kernel [54] from consideration.

### B. Stokes Solver

In the FIB method we obtain the fluid velocity  $\mathbf{v} = \eta^{-1} \mathcal{L}^{-1} \mathbf{g}$  by numerically solving the discrete steady Stokes equation

$$\begin{aligned} G\pi - \eta L\mathbf{v} &= \mathbf{g} = \mathcal{S}\mathbf{F} + \sqrt{\frac{2k_B T \eta}{\Delta V}} \tilde{\mathbf{D}}\mathbf{W} \\ D\mathbf{v} &= 0 \end{aligned} \quad (28)$$

using a preconditioned Krylov iterative solver [49]. Note that we can explicitly write  $\mathcal{L}^{-1}$  using the Schur complement of (28),

$$-\mathcal{L}^{-1} = L^{-1} - L^{-1}G(DL^{-1}G)^{-1}DL^{-1}. \quad (29)$$

In the continuum setting, and also in the discrete setting with periodic boundary conditions, the various operators commute and one can simplify  $\mathcal{L}^{-1} = -\mathbf{P}\mathbf{L}^{-1}$ , where  $\mathbf{P} = \mathbf{I} - \mathbf{G}(\mathbf{D}\mathbf{G})^{-1}\mathbf{D}$  is the  $L_2$  projection operator onto the subspace of (discretely) divergence free vector fields. In general, however, for many spatial discretizations, including the one we use, the operators do *not* commute and one must keep the full form (29) [68, 69].

### C. Discrete Fluctuation Dissipation Balance

The spatially-discretized equation of motion for the particles has the same form as the continuum (18), and is an instance of (3) with the identification

$$\begin{aligned} \mathcal{M} &= \eta^{-1} \mathcal{J}\mathcal{L}^{-1} \mathcal{S} \\ \mathcal{M}^{\frac{1}{2}} &= (\eta \Delta V)^{-\frac{1}{2}} \mathcal{J}\mathcal{L}^{-1} \tilde{\mathbf{D}}. \end{aligned} \quad (30)$$

Note that the key relation (20) continues to hold,  $-\mathcal{L}^{-1} \mathbf{L} \mathcal{L}^{-1} = \mathcal{L}^{-1}$ , which follows directly from (29).

This can be used to show that (2) is satisfied

$$\begin{aligned} & \mathcal{M}^{\frac{1}{2}} \left( \mathcal{M}^{\frac{1}{2}} \right)^T \\ &= -(\eta \Delta V)^{-1} \left[ \mathcal{J} \mathcal{L}^{-1} \left( \tilde{D} \tilde{D}^T \right) \mathcal{L}^{-1} (\Delta V \mathcal{S}) \right] \\ &= -\eta^{-1} \mathcal{J} (\mathcal{L}^{-1} \mathcal{L} \mathcal{L}^{-1}) \mathcal{S} = \eta^{-1} \mathcal{J} \mathcal{L}^{-1} \mathcal{S} = \mathcal{M}, \end{aligned} \quad (31)$$

where we made use of  $\mathcal{J}^T = \Delta V \mathcal{S}$ . Note that these relations are independent of the boundary conditions and thus (31) holds in confined systems.

#### IV. TEMPORAL DISCRETIZATION

In this section we introduce our approach for temporal integration of the spatially-discretized equations of motion. A significant challenge is accurately capturing the thermal drift present in the Ito interpretation,  $\partial_{\mathbf{q}} \cdot \mathcal{M}(\mathbf{q})$ , without which the system would not obey fluctuation-dissipation balance. This requires consistently discretizing the kinetic integral, which can be done in multiple dimensions using a Fixman predictor corrector scheme [56]. The Fixman scheme, however, requires applying the action of the inverse of the mobility (or, equivalently, the action of the square root of the inverse of the mobility), which is a complicating and a potentially expensive step [20]. Note that in certain cases, notably, for translationally-invariant situations such as periodic systems, the divergence of mobility vanishes and one can use a simple Euler-Maruyama integrator, as done in the work of Atzberger and collaborators [17]. This is not applicable to confined systems, however, and here we employ the Random Finite Difference (RFD) approach introduced in Section IID 2.

Below we use the superscript  $n$  to denote the current time step and quantities evaluated at the beginning of the current time step, and superscript  $n+1$  for the updated quantities at the end of the time step. Quantities estimated at the midpoint of the time step are denoted with superscript  $n+\frac{1}{2}$ . For example,  $\mathcal{M}^{n+\frac{1}{2}} \equiv \mathcal{M} \left( \mathbf{q}^{n+\frac{1}{2}} \right)$  denotes a midpoint approximation of the mobility. We develop two temporal integrators, a first-order simple midpoint method that requires only a single Stokes solve per time step, and an improved midpoint midpoint scheme that achieves second-order accuracy in the additive-noise (linearized) case at the cost of requiring two Stokes solves per time step. Which scheme allows for better tradeoff between accuracy and efficiency will depend on the specific problem at hand, and in particular, on the time step limitations imposed by stability considerations.

##### A. Simple midpoint scheme

A direct application of the RFD approach to integrating (18) would require evaluating the action of the mobility at two different configurations and thus at least two

Stokes solves per time step. In order to avoid using a separate Stokes solver just to obtain the thermal drift term, we take an alternative approach and split the thermal drift into two pieces,

$$\begin{aligned} \eta \partial_j \mathcal{M}_{ij}(\mathbf{q}) &= \partial_j \left( \mathcal{J}_{ik}(\mathbf{q}) \mathcal{L}_{kl}^{-1} \mathcal{S}_{lj}(\mathbf{q}) \right) = \\ &= (\partial_j \mathcal{J}_{ik}(\mathbf{q})) \mathcal{L}_{kl}^{-1} \mathcal{S}_{lj}(\mathbf{q}) + \mathcal{J}_{ik}(\mathbf{q}) \mathcal{L}_{kl}^{-1} (\partial_j \mathcal{S}_{lj}(\mathbf{q})), \end{aligned} \quad (32)$$

where we use the implied summation convention. The two pieces can be handled separately, and only require the derivatives of  $\mathcal{J}$  and  $\mathcal{S}$ . We approximate the term  $\partial_j \mathcal{J}_{ik}(\mathbf{q})$  using a predictor-corrector approach in the spirit of Runge-Kutta algorithms such as the Euler-Heun temporal integrator for Stratonovich equations [75]. We use an RFD of the form (25) with  $\Delta \mathbf{q} \sim \Delta \mathbf{p}$  to calculate the term  $\partial_j \mathcal{S}_{lj}(\mathbf{q})$ .

Our basic temporal integrator for the spatially-discretized equations (18) consists of first solving the steady Stokes equations with a random forcing,

$$\begin{aligned} -\eta \mathcal{L} \mathbf{v} + \mathbf{G} \pi &= \mathcal{S}^n \mathbf{F}^n + \sqrt{\frac{2\eta k_B T}{\Delta t \Delta V}} \tilde{\mathbf{D}} \mathbf{W}^n \\ &+ \frac{k_B T}{\delta} \left[ \mathcal{S} \left( \mathbf{q}^n + \frac{\delta}{2} \tilde{\mathbf{W}}^n \right) - \mathcal{S} \left( \mathbf{q}^n - \frac{\delta}{2} \tilde{\mathbf{W}}^n \right) \right] \tilde{\mathbf{W}}^n, \end{aligned} \quad (33)$$

and then advecting the particles with the computed velocity field using a midpoint predictor-corrector scheme,

$$\mathbf{q}^{n+\frac{1}{2}} = \mathbf{q}^n + \frac{\Delta t}{2} \mathcal{J}^n \mathbf{v} \quad (34)$$

$$\mathbf{q}^{n+1} = \mathbf{q}^n + \Delta t \mathcal{J}^{n+\frac{1}{2}} \mathbf{v}. \quad (35)$$

Here  $\mathbf{W}^n$  is a random vector of i.i.d. standard Gaussian random numbers that represent stochastic fluxes of momentum, with  $\mathbf{W}^n / \sqrt{\Delta t}$ , loosely speaking, being a temporal discretization of  $\mathcal{W}(t)$ . The auxiliary displacement  $\tilde{\mathbf{W}}^n$  is a vector of  $nd$  i.i.d. standard Gaussian variates. The parameter  $\delta$  should be as small as possible while still resolving to numerical roundoff the length scale over which  $\mathcal{S}$  varies; we use  $\delta \approx 10^{-6}h$ , where  $h$  is the grid spacing.

The first-order midpoint temporal integrator (33)-(35) has the advantage that we can recreate the stochastic drift  $\partial_{\mathbf{q}} \cdot \mathcal{M}$  by performing only two additional spreading operations and one local averaging operation per time step, in addition to the required Stokes solve. We use a midpoint corrector step (35) because in the absence of the RFD term it gives the correct diffusion coefficient for freely-diffusing single particles, *regardless* of the time step size. Namely, for any choice of  $\Delta t$ , the second moment of the stochastic increment of the particle positions is in agreement with the Einstein formula for the diffusion coefficient,

$$\begin{aligned} \text{Var}(\mathbf{q}^{n+1} - \mathbf{q}^n) &= 2\Delta t k_B T \eta^{-1} \left( \mathcal{J}^{n+\frac{1}{2}} \mathcal{L}^{-1} \mathcal{S}^{n+\frac{1}{2}} \right) \\ &= 2\Delta t k_B T \mathcal{M}^{n+\frac{1}{2}}, \end{aligned} \quad (36)$$

up to correction terms coming from the RFD term in the second line of (33). In section VB, we confirm that this

property continues to hold to very high accuracy when the RFD is included, even for relatively large  $\Delta t$ . Note that a trapezoidal scheme that replaces the term  $\mathcal{J}^{n+\frac{1}{2}}\mathbf{v}$  in (35) with  $(\mathcal{J}^n + \mathcal{J}^{n+1})\mathbf{v}/2$  does not have the property (36) and only gives the correct diffusion coefficient for small  $\Delta t$ .

The predictor corrector steps (34)-(35) reproduce the first term on the right hand side of (32). The added stochastic force in the Stokes solve generates the thermal forcing (16), which appears in the second term on the right hand side of (32), in expectation to order  $\delta^2$ ,

$$\begin{aligned} & \frac{k_B T}{\delta} \left\langle \mathcal{S}_{lj} \left( \mathbf{q}^n + \frac{\delta}{2} \widetilde{\mathbf{W}}^n \right) \widetilde{\mathbf{W}}_j^n - \mathcal{S}_{lj} \left( \mathbf{q}^n - \frac{\delta}{2} \widetilde{\mathbf{W}}^n \right) \widetilde{\mathbf{W}}_j^n \right\rangle \\ &= k_B T (\partial_k \mathcal{S}_{lj}(\mathbf{q}^n)) \langle \widetilde{\mathbf{W}}_k^n \widetilde{\mathbf{W}}_j^n \rangle + O(\delta^2) \\ &= k_B T \partial_j \mathcal{S}_{lj}(\mathbf{q}^n) + O(\delta^2). \end{aligned} \quad (37)$$

In Appendix A we demonstrate that the simple midpoint scheme (33)-(35) is a first-order weak integrator for the equations of Brownian dynamics (18).

### B. Improved midpoint scheme

It is possible to obtain second order accuracy in the additive-noise (linearized) approximation by using an additional Stokes solve in the corrector stage, as summarized by

$$\begin{aligned} -\eta \mathbf{L} \mathbf{v} + \mathbf{G} \pi &= \mathcal{S}^n \mathbf{F}^n + \sqrt{\frac{4\eta k_B T}{\Delta t \Delta V}} \widetilde{\mathbf{D}} \mathbf{W}^{n,1} \\ \mathbf{D} \mathbf{v} &= 0 \\ \mathbf{q}^{n+\frac{1}{2}} &= \mathbf{q}^n + \frac{\Delta t}{2} \mathcal{J}^n \mathbf{v} \quad (\text{predictor}) \\ -\eta \mathbf{L} \tilde{\mathbf{v}} + \mathbf{G} \tilde{\pi} &= \mathcal{S}^{n+\frac{1}{2}} \mathbf{F}^{n+\frac{1}{2}} + \sqrt{\frac{\eta k_B T}{\Delta t \Delta V}} \widetilde{\mathbf{D}} (\mathbf{W}^{n,1} + \mathbf{W}^{n,2}) \\ &+ \frac{k_B T}{\delta} \left[ \mathcal{S} \left( \mathbf{q}^n + \frac{\delta}{2} \widetilde{\mathbf{W}}^n \right) - \mathcal{S} \left( \mathbf{q}^n - \frac{\delta}{2} \widetilde{\mathbf{W}}^n \right) \right] \widetilde{\mathbf{W}}^n \\ \mathbf{D} \tilde{\mathbf{v}} &= 0 \\ \mathbf{q}^{n+1} &= \mathbf{q}^n + \Delta t \mathcal{J}^{n+\frac{1}{2}} \tilde{\mathbf{v}} \quad (\text{corrector}). \end{aligned} \quad (38)$$

Here the independent random variables  $\mathbf{W}^{n,1}$  and  $\mathbf{W}^{n,2}$  represent the two independent Wiener increments over each half of the time step, as explained in more detail in Ref. [68]. Note that by using a midpoint corrector step we ensure that the property (36) continues to hold. Here we only include an RFD term in the corrector step and use the initial position of the particle in the RFD term. One can also use  $\mathbf{q}^{n+\frac{1}{2}}$  instead of  $\mathbf{q}^n$  but this gains no additional accuracy.

Note that the scheme (38) is still only first order weakly accurate (see Appendix A) because the noise in (18) is multiplicative. Achieving second-order weak accuracy in the nonlinear case requires more sophisticated stochastic Runge-Kutta schemes [76]. However, we will demonstrate in Sec. VD that the improved midpoint scheme

can sometimes give results which are significantly more accurate because the scheme (38) can be shown to be second order weakly accurate for the linearized (additive-noise) equations of Brownian dynamics [68]. The improved midpoint scheme may also give improved stability in certain cases, as we observe numerically in Section VE. Note, however, that both midpoint schemes are explicit and are thus subject to stability limits on  $\Delta t$ , dictated by the stiffness of the applied forces  $\mathbf{F}(\mathbf{q})$ .

## V. RESULTS

In this section we test the performance of the FIB by simulating a number of scenarios of increasing complexity. We start by confirming that our spatial discretization gives a mobility in agreement with known results for a single particle in a slit channel. We then confirm that our temporal integrators preserve the correct Gibbs-Boltzmann distribution for both single and multiparticle systems. After also verifying that the FIB method correctly reproduces the dynamical correlations between particles in the presence of shear flow and hydrodynamic interactions, we compare our method to standard Brownian Dynamics on the nonequilibrium dynamics of a colloidal cluster. Unless otherwise mentioned, the tests were conducted using the simple midpoint temporal integrator (33)-(35).

We have implemented the FIB algorithm in the open source code IBAMR [77], a parallel implementation of the immersed boundary method. The state-of-the-art multigrid-based iterative Stokes solvers [49] implemented in IBAMR enable us to efficiently solve the steady Stokes equations for any combination of periodic, no-slip or free-slip boundaries on the side of a rectangular domain, including in the presence of thermal fluctuations [69]. Although IBAMR supports adaptive mesh refinement (AMR) for deterministic time-dependent problems, at present only uniform grids are supported for steady-state flows with fluctuations. Unless otherwise specified, the simulations reported here were performed using the IBAMR implementation of the FIB method.

For periodic domains, no iterative solvers are necessary for uniform grids since the discrete Fourier transform diagonalizes the discrete Stokes equations and the Fast Fourier Transform (FFT) can be used to solve the steady Stokes equations very efficiently. This was used by some of us to solve the inertial fluid-particle equations efficiently on Graphical Processing Units (GPUs), as implemented in the open-source *fluam* CUDA code [19]. Implementing the FIB method in *fluam* amounted to simply changing the temporal integration scheme (for both the fluid and the particle dynamics) to the midpoint scheme (33)-(35), while reusing the core numerical implementation. Note that we only use FFTs as a linear solver for the discrete Stokes equations, similar to what is done in SIBM [50]. This means that the IBAMR and *fluam* codes give the same results for periodic sys-

tems to within solver tolerances. For periodic systems at zero Reynolds number flow a much higher (spectral) spatial accuracy can be accomplished by using a Fourier representation of the velocity and pressure, as done by Keaveny [20]. In fact, with proper care in choosing the number of Fourier modes kept and the help of the non-uniform FFT algorithm [78] one can construct a spatial discretization where the truncation error is at the level of roundoff tolerance [59]. In the presence of simple confinement such as a slit channel with only two walls, a Fourier representation can be used in the directions parallel to the channel walls, along with a different basis for the direction perpendicular to the walls. Here we do not explore such specialized geometries and use a finite-volume Stokes solver to handle more general combinations of boundary conditions.

While the different tests performed have different relevant timescales, there is an important common timescale of diffusion given by the typical time it takes a free particle to diffuse a distance  $h$ , where  $h$  is the grid spacing. The typical value of the diffusion coefficient of a single spherical particle in a translationally-invariant system can be obtained from the mobility  $\mu$  via the Stokes-Einstein relation,  $\chi_{\text{self}} = k_B T \mathbf{M}_{\text{self}} = k_B T \mu \mathbf{I} = \chi \mathbf{I}$ , and leads to  $\chi \approx k_B T / (6\pi\eta a)$  in three dimensions, and  $\chi \approx k_B T (4\pi\eta)^{-1} \ln(L/3.708a)$  in two dimensions [45], where we recall that  $a$  is the effective hydrodynamic radius of a blob and  $L$  is the length of the periodic domain. In three dimensions there are well-known finite size corrections to the mobility that are taken into account in the calculations below [16, 19, 65, 73]. Based on the estimated diffusion coefficient we can define a dimensionless time step size through the diffusive Courant number

$$\beta = \frac{2\chi}{h^2} \Delta t.$$

This dimensionless number should be kept small (e.g.,  $\beta \lesssim 0.25$ ) in order to prevent a particle from jumping more than one grid cell during a single time step. Note that this time step limitation is much weaker than the corresponding limitation in methods that resolve the inertial dynamics, such as the Inertial Coupling method [19]. Resolving the time scale of the momentum diffusion requires keeping  $\beta_\nu = 2\nu\Delta t/h^2 = \text{Sc}\beta$  small, which requires a time step on the order of  $\text{Sc} \sim 10^3 - 10^4$  smaller than the FIB method. Note, however, that in applications the time step may further be limited by other factors such as the presence of stiff inter-particle potentials, as we discuss further in Section V E.

### A. Mobility in a Slit Channel

The mobility of a single particle in a slit channel is affected by the presence of the two walls. We estimate this effect by placing a particle at multiple points across a  $128h \times 128h \times 32h$  channel with planar no-slip walls at  $z = 0$  and  $z = 32h$ , and periodic boundaries along the

$x$  and  $y$  directions. For each position of the blob, a unit force is applied either parallel and perpendicular to the wall, the Stokes system (17) without the stochastic momentum flux is solved, and the resulting particle velocity is calculated, giving the parallel  $\mu_{\parallel}$  and perpendicular  $\mu_{\perp}$  mobilities. The results of these calculations are reported in Fig. 1.

Unlike the case of a single no-slip boundary [32], writing down an analytical solution for slit channels is complex and requires numerically-evaluating the coefficients in certain series expansions [37]. For the parallel component of the mobility, Faxen has obtained exact series expansions for the mobility at the half and quarter channel locations,

$$\begin{aligned} \mu_{\parallel} \left( H = \frac{L}{2} \right) &= \frac{1}{6\pi\eta a} \left[ 1 - 1.004 \frac{a}{H} + 0.418 \frac{a^3}{H^3} \right. \\ &\quad \left. + 0.21 \frac{a^4}{H^4} - 0.169 \frac{a^5}{H^5} + \dots \right] \\ \mu_{\parallel} \left( H = \frac{L}{4} \right) &= \frac{1}{6\pi\eta a} \left[ 1 - 0.6526 \frac{a}{H} + 0.1475 \frac{a^3}{H^3} \right. \\ &\quad \left. - 0.131 \frac{a^4}{H^4} - 0.0644 \frac{a^5}{H^5} + \dots \right] \end{aligned}$$

where  $H$  denotes the distance from the blob to the nearest wall, and  $L$  is the distance between the walls. Here we neglect the corrections coming from the use of periodic boundary conditions in the  $x$  and  $y$  directions. As seen in Fig. 1, the exact results of Faxen are in excellent agreement with the numerical mobilities.

For other positions of the blob, we employ two different approximations. Both of these make use the Modified Coherent Superposition Assumption (MCSA) approximation to the unwieldy full expression for the mobility [37]. This approach considers an infinite sum of reflections of the single-wall solutions in another wall [79]. In Fig. 1 we show two MCSA approximations which we evaluated using (c.f. Eq. (9) in Ref. [79])

$$\begin{aligned} \frac{\mu^{(2)}}{\mu_0} &= \left\{ 1 + \sum_{n=0}^{\infty} (-1)^n \left[ \frac{\mu_0}{\mu^{(1)}(nL + H)} - 1 \right] + \right. \\ &\quad \left. + \sum_{n=1}^{\infty} (-1)^n \left[ \frac{\mu_0}{\mu^{(1)}((n+1)L - H)} - 1 \right] \right\}^{-1} \quad (39) \end{aligned}$$

where  $\mu^{(2)}$  is either the parallel  $\mu_{\parallel}^{(2)}$  or the perpendicular  $\mu_{\perp}^{(2)}$  mobility in the slit channel,  $\mu_0$  is the mobility in an unbounded domain, and  $\mu^{(1)}$  is the parallel or perpendicular single-wall mobility. Note that  $\mu^{(2)} \approx \mu^{(1)}$  when the distance between the walls is very large,  $L \gg H \gg a$ , as it must. Both of the MCSA approximations are for an infinite slit geometry, whereas we use periodic boundary conditions in the directions parallel to the walls; we expect this has a small effect on the value of the mobility

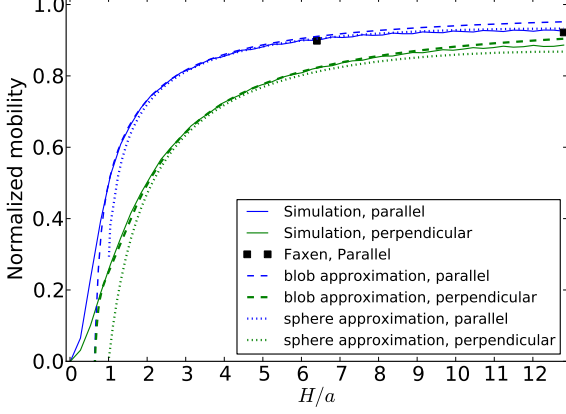


Figure 1: Mobility (relative to unbounded flow) of a blob of hydrodynamic radius  $a$  in a slit channel of thickness  $\sim 25.5a$  in the directions parallel (blue lines and symbols) and perpendicular (green lines) to the confining no-slip walls as a function of the distance  $H$  to the wall (expressed here in terms of the blob hydrodynamic radius  $a$ ), in three dimensions. Note that small oscillations appear due to numerical grid artifacts. For the parallel mobility, simulation is in excellent agreement with two exact results obtained by Faxen (symbols), and over the range of distances where the blob does not overlap the wall, the results are in good agreement with the MCSA approximation for a blob in a channel (dashed lines, see eq. (40)). Also shown is the MCSA approximation for a hard sphere in a channel (dotted lines, see eq. (41, 42)) [79].

calculated due to hydrodynamic screening, as evidenced by the match with the exact results by Faxen.

We compare our numerical mobility to two different evaluations of (39), based on two different approximation for the single-wall mobility  $\mu^{(1)}$ . The first is given by Swan and Brady [32],

$$\frac{\mu_{\perp}^{(1)}(H)}{\mu_0} = 1 - \frac{9a}{8H} + \frac{a^3}{2H^3} - \frac{a^5}{8H^5} \quad (40)$$

$$\frac{\mu_{\parallel}^{(1)}(H)}{\mu_0} = 1 - \frac{9a}{16H} + \frac{2a^3}{16H^3} - \frac{a^5}{16H^5},$$

as a generalization of the Rotne-Prager tensor using Blake’s image construction for a single wall [60]. As such, we expect this result to be accurate for blob particles near a single wall, and we see good agreement in Fig. 1. We also use a second expression for  $\mu^{(1)}$  which more closely approximates a hard sphere. For this approximation, the perpendicular mobility is given by a semi-empirical rational relation approximation to an exact series of Brenner [80],

$$\frac{\mu_{\perp}^{(1)}(H)}{\mu_0} = \frac{6\left(\frac{H}{a}\right)^2 + 2\left(\frac{H}{a}\right)}{6\left(\frac{H}{a}\right)^2 + 9\left(\frac{H}{a}\right) + 2}. \quad (41)$$

The hard sphere approximation to the parallel single wall mobility is given by a combination of a near-wall expres-

sion derived using lubrication theory and a truncated expansion in powers of  $a/H$  which is more accurate further from the wall. The near-wall calculation involves a complicated expression which we do not reproduce here (see [81]), and it is used when  $H - a \leq 0.05a$ . When the blob is further from the wall, we calculate the single wall parallel mobility from the exact power series expansion truncated to fifth order [82],

$$\frac{\mu_{\parallel}^{(1)}(H)}{\mu_0} = 1 - \frac{9a}{16H} + \frac{1a^3}{8H^3} - \frac{45a^4}{256H^4} - \frac{a^5}{16H^5}. \quad (42)$$

Both MCSA (39) approximations are seen to be in very good agreement with our numerical results away from the wall in Fig. 1. Near the wall, the fact that we use a minimally resolved “blob” model becomes relevant, and the numerical results agree more with (40) than with (41,42). The approximations (40) and especially (41,42) are intended to work only for  $H > a$ . In particular, the Swan-Brady Rotne-Prager-Blake tensor only ensures an SPD mobility when the blobs do not overlap the wall or each other. By contrast, our numerical calculation does not diverge when the blob overlaps the wall, giving instead a mobility that smoothly decays to zero as the centroid of the blob approaches the wall, and is SPD for all blob configurations as long as all blob centroids are inside the channel. Close to the wall our numerical results are expected to be in close agreement with the Rotne-Prager-Yamakawa-Blake tensor [83], which is, unfortunately, not available in closed form.

## B. Diffusion Coefficient

As explained in Section IV A, we chose the midpoint form of the predictor corrector (34,35), because this gives an accurate diffusion coefficient even for large time step size  $\Delta t$ . Here we confirm this by numerically estimating the time-dependent diffusion coefficient of a single freely-diffusing particle in a two dimensional periodic domain

$$\chi(s) = \frac{1}{2ds} \left\langle \|\mathbf{q}(t+s) - \mathbf{q}(t)\|^2 \right\rangle$$

for a range of time step sizes. For comparison, we also try a simple trapezoidal predictor-corrector scheme that replaces (34,35) with

$$\mathbf{q}^{*,n+1} = \mathbf{q}^n + \Delta t \mathcal{J}^n \mathbf{v}$$

$$\mathbf{q}^{n+1} = \mathbf{q}^n + \frac{\Delta t}{2} (\mathcal{J}^n + \mathcal{J}^{*,n+1}) \mathbf{v}. \quad (43)$$

This scheme is also a first-order weakly accurate integrator, but does not satisfy the property (36).

Figure 2 shows that the midpoint predictor corrector (34,35) gives a diffusion coefficient that agrees with the theoretical result  $\chi(s) = k_B T \mu$  independent of  $s$  to within statistical error for time step sizes as large as  $\beta = \Delta t/\tau = 2\chi\Delta t/h^2 = 1.43$ , where  $\tau$  is the natural

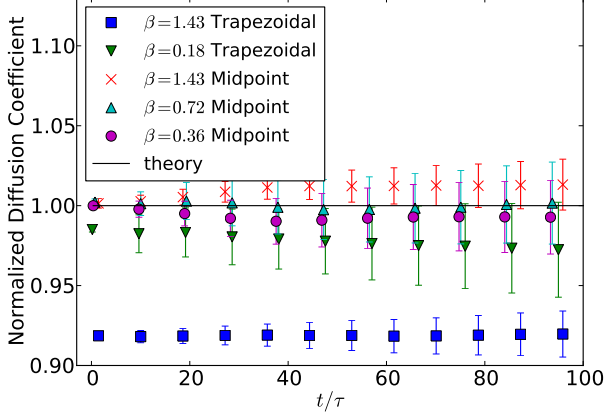


Figure 2: Normalized diffusion coefficient for multiple time step sizes using the midpoint (34,35) or the trapezoidal (43) predictor-corrector schemes.

diffusive time scale for this test. By contrast, the trapezoidal scheme (43) introduces a measurable truncation error already for  $\beta \gtrsim 0.2$ . Both schemes include an RFD term to approximate the (small) drift term present due to the discretization showing that the RFD term does not ruin the accuracy of the diffusion coefficient for the midpoint scheme.

### C. Thermodynamic Equilibrium

One of the most important requirements on any scheme that couples fluctuating hydrodynamics to immersed particles is to reproduce the Gibbs-Boltzmann distribution (4) at thermodynamic equilibrium, independent of any dynamical parameters such as viscosity. In prior work [19], we confirmed that when fluid and particle inertia are consistently included in the formulation, the numerical method reproduces the correct equilibrium distribution for both the particle positions and the appropriate Maxwell-Boltzmann distribution for the particle velocities. In the overdamped limit considered here there are no velocity degrees of freedom, but the method should still reproduce the correct Gibbs-Boltzmann distribution (4) for sufficiently small time steps. In this section we consider several scenarios and verify that the FIB method correctly reproduces the theoretical equilibrium distribution. As we demonstrate next, in the case of a non-constant mobility this necessitates the proper inclusion of the stochastic drift terms using the specialized temporal integration techniques we developed in Section IV.

#### 1. Free Diffusion

In the continuum setting, for a single particle in a periodic system translational invariance implies that the mobility does not depend on the position of the particle, and therefore  $\partial_q \cdot \mathcal{M} = 0$ . However, upon spatial discretization, translational invariance is broken by the presence of a fixed Eulerian grid on which the fluid equation is solved. Even though the Peskin kernels give excellent translational invariance of the mobility, there is still a fraction to a few percent (depending on the kernel) variation in the mobility as the particle position shifts relative to the underlying grid. Here we show that our midpoint temporal integrators correct for this and ensure a uniform equilibrium distribution for the position of freely-diffusing particles.

In this test, 3000 particles are allowed to diffuse freely in a periodic two-dimensional domain of size  $16h \times 16h$ . Because the particles do not exert forces on each other, each of the particles is statistically identical to an isolated particle diffusing in the same domain (even though the particles are not independent because of the hydrodynamic interactions [72]), and at equilibrium their positions should be independent and uniformly distributed in the periodic domain. A small time step size corresponding to  $\beta \approx 0.01$  is used to approach the limit  $\Delta t \rightarrow 0$ . The three-point Peskin kernel is used in order to maximize the lack of translational invariance.

For testing purposes, we dropped the RFD and corrector stages in the simple midpoint scheme (33)-(35) to obtain the Euler-Maruyama integrator,

$$\begin{aligned} -\eta L\mathbf{v} + \mathbf{G}\pi &= \mathcal{S}^n \mathbf{F}^n + \sqrt{\frac{2k_B T}{\Delta t \Delta V}} \tilde{\mathbf{D}} \mathbf{W}^n \\ \mathbf{D}\mathbf{v} &= 0 \\ \mathbf{q}^{n+1} &= \mathbf{q}^n + \Delta t \mathcal{J}^n \mathbf{v}. \end{aligned} \quad (44)$$

Note that this temporal integrator is inconsistent with the kinetic interpretation of the noise term, i.e., it is not consistent with the Fokker-Planck equation (5); it is biased even in the limit  $\Delta t \rightarrow 0$ .

The Euler-Maruyama method was compared with our midpoint scheme (33)-(35) by computing an empirical histogram for the equilibrium distribution of the position of a particle inside a cell (due to translational invariance of the periodic grid the distribution is the same in all grid cells). The results in Fig. 3 show small but clear artifacts in the equilibrium distribution when using the Euler-Maruyama (44) scheme, specifically, the particle is more likely to be found near the corners of the grid cell instead of the center of the grid cell. By contrast, our consistent integrator (33)-(35) give a uniform distribution for the position of the particle for sufficiently small time step sizes; the same is true for the improved integrator (38), not shown.

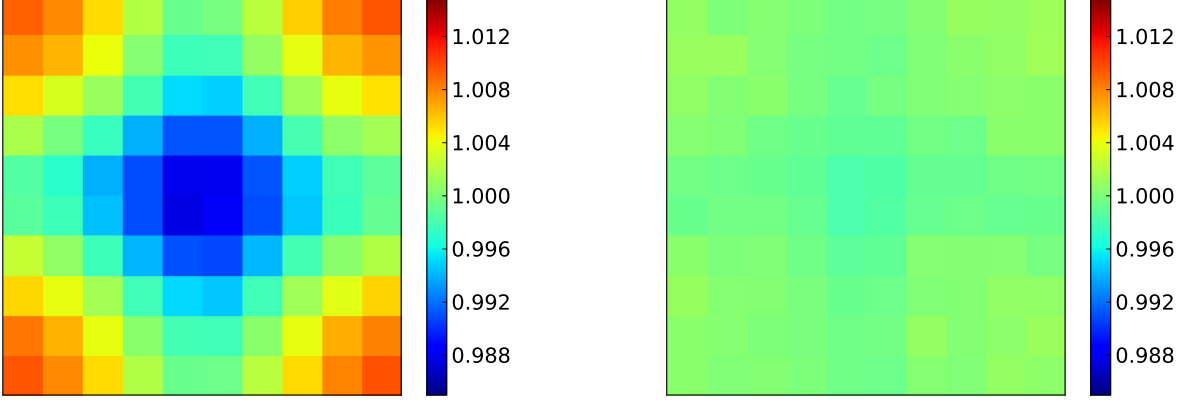


Figure 3: (*Left panel*) Normalized equilibrium probability distribution for finding a free particle at a particular position inside a grid cell when using the Euler-Maruyama scheme (44). A slightly nonuniform distribution is observed, in disagreement with the correct uniform Gibbs-Boltzmann distribution. This error does *not* vanish in the limit  $\Delta t \rightarrow 0$ . (*Right panel*) Using the midpoint scheme (33)-(35) preserves the correct distribution. The small residual artifacts disappear in the limit  $\Delta t \rightarrow 0$ . The same color scale (with variation in the range  $0.985 - 1.015$ ) is used for both panels.

## 2. Diffusion in a slit channel

One key strength of the FIB method is the ability to handle non-periodic boundary conditions. In this test particles are placed in a two-dimensional channel and allowed to diffuse freely. When a particle comes within a cutoff range  $w$  from one of the two no-slip walls, it is repelled with a harmonic potential with spring stiffness  $k$ ,

$$U(H) = \frac{k}{2}(H - w)^2 \quad \text{if } H \leq w \quad \text{and zero otherwise,} \quad (45)$$

where  $H$  is the distance of the particle from the wall. The total potential for the equilibrium distribution is the sum of the top and bottom wall potentials. A long equilibrium run is performed in order to compute an empirical histogram for the marginal equilibrium distribution  $P(H)$  for finding a particle at a given distance  $H$  from the nearest wall (note that all particles are statistically identical). We perform the simulations in two dimensions in order to maximize the statistical accuracy. The values of the simulation parameters are given in Table I. Note that here we employ a relative large time step size in order to test the robustness of our temporal integrators.

As illustrated in Fig. 4, the results of the midpoint algorithm (33) with 100 particles compares favorably to the correct Gibbs-Boltzmann distribution  $P(H) = Z^{-1} \exp(-U(H)/k_B T)$ . We also test the biased Euler-Maruyama scheme (44) for a single particle. This scheme does not reproduce the thermal drift term from Eq. (18), and thus yields an unphysical result where particles are more likely to be found near the boundaries (see also discussion in Section III.C in Ref. [37]).

Number of particles	100 (midpoint) or 1 (Euler)
wall “spring” constant $k$	$6 (k_B T/h^2)$
wall potential range $w$	$2h$
dimensionless time step size $\beta$	0.023
domain width $L_x$	$8h$
domain height $L_y$	$16h$

Table I: Parameters used for the slit channel simulation results shown in Fig. 4.

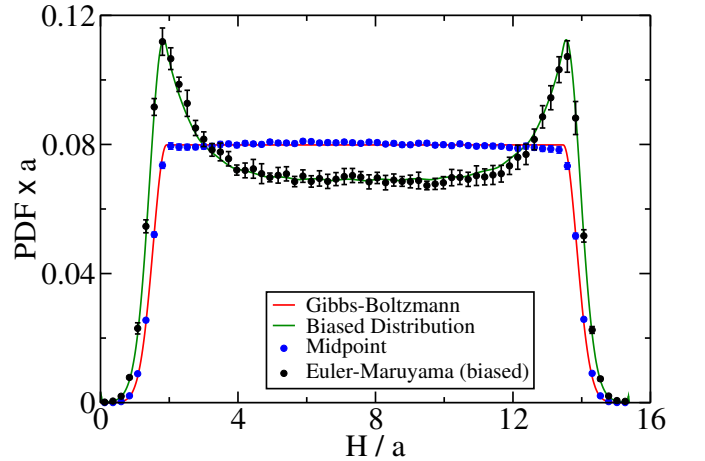


Figure 4: Probability distribution of the distance  $H$  to one of the walls for a freely-diffusing single blob (Euler-Maruyama scheme (44)), as well as many non-interacting (midpoint scheme (33)) blobs, in a two dimensional slit channel. The correct (unbiased) (4) and the biased (47) Gibbs-Boltzmann distribution are shown for comparison.

In fact, the equilibrium distribution preserved by the biased scheme (44) in the limit  $\Delta t \rightarrow 0$  can be calculated analytically for a single particle. For one particle in a slit channel, the  $x$  and  $y$  components of (1) decouple, and the only interesting dynamics occurs in the direction perpendicular to the channel walls. The Euler-Maruyama scheme (46) is consistent with the Ito equation

$$\frac{dH}{dt} = -\mu_{\perp}(H) U'(H) + \sqrt{2k_B T \mu_{\perp}(H)} \mathcal{W}_2(t). \quad (46)$$

By adding and subtracting  $k_B T \mu'_{\perp}(H)$  we can convert this into the kinetic stochastic interpretation,

$$\begin{aligned} \frac{dH}{dt} &= -\mu_{\perp}(H) \tilde{U}'(H) + \sqrt{2k_B T \mu_{\perp}(H)} \mathcal{W}_2(t) \\ &\quad + k_B T \mu'_{\perp}(H) \\ &= -\mu_{\perp}(H) \tilde{U}'(H) + \sqrt{2k_B T \mu_{\perp}(H)} \diamond \mathcal{W}_2(t), \end{aligned}$$

where the biased potential is

$$\tilde{U}(H) = U(H) + k_B T \ln(\mu_{\perp}(H)).$$

This shows that the Euler-Maruyama scheme (46) preserves the biased Gibbs-Boltzmann distribution corresponding to the biased potential  $\tilde{U}(H)$ ,

$$P_E(H) = \tilde{Z}^{-1} \exp\left(-\frac{\tilde{U}(H)}{k_B T}\right). \quad (47)$$

The biased distribution  $P_E(H)$  is shown in Fig. 4 with  $\mu_{\perp}$  calculated numerically (see Fig. 1). The biased distribution indeed matches the simulation results from the Euler-Maruyama scheme, confirming that the correct equilibrium distribution is not preserved without the RFD term and predictor-corrector steps. At the same time, we see that the temporal integrator (33)-(35) preserves the correct thermodynamic equilibrium distribution even in the presence of confinement.

### 3. Colloidal suspension

In this section we verify that our FIB algorithm gives the correct equilibrium distribution  $P(\mathbf{q})$  for a multi-particle system by computing the radial (pair) distribution function (RDF)  $g(r)$  for a periodic collection of  $N$  colloidal particles interacting with a pairwise repulsive truncated Lennard-Jones (LJ) potential  $V(r)$ ,

$$U(\mathbf{q}) = \sum_{i,j=1}^N V(\|\mathbf{q}_i - \mathbf{q}_j\|),$$

as described in more detail in Section 4.1 in Ref. [19]. The parameters used for these simulations are given in Table II, and the GPU-based code *fluam* with the three point kernel is used for these simulations [19]. In the left panel of Fig. 5 we compare  $g(r)$  between a simulation

grid spacing $\Delta x$	1
grid size	$32^3$
shear viscosity $\eta$	1
time step size $\Delta t$	Variable
temperature $k_B T$	$10^{-3}$
LJ strength $\epsilon$	$10^{-3}$
LJ / hydro diameter $\sigma$	2
number of particles $N$	1000 (dilute) or 3300 (dense)

Table II: Parameters used in the colloidal suspension equilibrium simulations shown in Fig. 5.

where the particles are immersed in an incompressible viscous solvent, and a standard computation of the equilibrium RDF using a Monte Carlo algorithm to sample the equilibrium distribution (4). We test the FIB algorithm at two different densities, a dilute suspension corresponding to a packing fraction based on the LJ diameter of  $\phi \approx 0.13$ , and a dense suspension (close to the freezing point) at packing fraction  $\phi \approx 0.42$ . Note that while the minimally-resolved model here cannot accurately model the dynamics (hydrodynamic interactions) at high packing fractions [31, 51], we do obtain the correct equilibrium properties because our formulation and numerical scheme obey discrete fluctuation-dissipation balance for any interaction potential and any viscosity.

As seen in Fig. 5, we obtain excellent agreement with the Monte Carlo calculations even for time steps close to the stability limit. The Brownian time scale here is [101]

$$\tau_B = \frac{a^2}{\chi} = \frac{6\pi a^3 \eta}{k_B T} \approx 2 \cdot 10^4,$$

and the time step size is primarily limited (to  $\Delta t \lesssim 100$ , corresponding to  $\beta = 0.005$ , for the dilute suspension, and  $\Delta t \lesssim 50$  for the denser suspension) by stability requirements relating to the presence of the stiff LJ repulsion between the particles. Note that the time step size in these simulations is substantially larger than those required in the Inertial Coupling scheme developed by some of us in Ref. [19] (there, a time step of  $\Delta t = 1$  was used).

### D. Particles in Shear Flow

In this section we verify the the FIB method correctly models the *dynamics* of hydrodynamically-interacting Brownian particles by computing time correlation functions of the positions of particles in shear flow. Particles are anchored with a harmonic spring to their initial locations and subjected to shear flow, as can be experimentally realized by using optical tweezers to apply the potential [84]. Brammert, Holzer, and Zimmerman have performed theoretical analysis of this system [85, 86] and provide explicit expressions used to test the accuracy of our scheme. The numerical results presented below



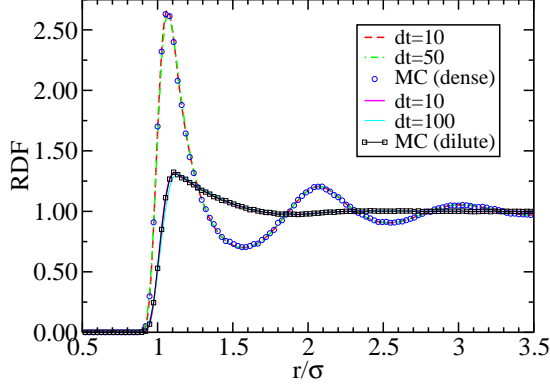


Figure 5: Radial pair correlation function  $g(r)$  for a suspension of particles interacting with repulsive Lennard-Jones potentials at packing fractions  $\phi \approx 0.13$  (dilute) and  $\phi \approx 0.42$  (dense). Results from two different time step sizes are compared to Monte Carlo (MC) simulations.

demonstrate the ability of our midpoint schemes to correctly reproduce the effect of hydrodynamic interactions between distinct immersed particles.

Note that it is not possible to have an unbounded system in a finite-volume approach; a finite system is necessary and it is most convenient to use a large but finite periodic system [102]. In these tests, we add a background shear flow with velocity  $\mathbf{u}$  to the *periodic* fluctuating component  $\mathbf{v}$  calculated by the steady Stokes solver; this mimics common practice in Brownian dynamics simulations of polymer chains in flow [26]. We will define  $y$  as the direction of shear, and  $x$  as the direction of flow. The background flow is of the form  $\mathbf{u}(x, y) = (\dot{\gamma}y, 0, 0)$  for some constant  $\dot{\gamma}$ . Note that the total flow  $\mathbf{u} + \mathbf{v}$  is a solution to the Stokes equations with the same forces that generated  $\mathbf{v}$ , but with boundary conditions modified to match the added background flow. The resulting velocity of the particle is then  $\mathcal{J}(\mathbf{q})\mathbf{v} + \mathcal{J}(\mathbf{q})\mathbf{u}$ . With a spherically symmetric kernel and the constant-shear flow  $\mathbf{u}$ , we have  $\mathcal{J}(\mathbf{q})\mathbf{u} = \mathbf{u}(\mathbf{q})$ . To implement the addition of the background flow, we calculate  $\mathcal{J}\mathbf{v}$  without any modification for the shear flow, and then separately add  $\mathbf{u}(\mathbf{q})$ . The temporal scheme is then the same as (33)-(35) but with  $\mathcal{J}^n\mathbf{v}$  replaced by  $\mathcal{J}^n\mathbf{v} + \mathbf{u}(\mathbf{q}^n)$  and likewise  $\mathcal{J}^{n+\frac{1}{2}}\mathbf{v}$  is replaced by  $\mathcal{J}^{n+\frac{1}{2}}\mathbf{v} + \mathbf{u}(\mathbf{q}^{n+\frac{1}{2}})$ . Note that here  $\mathbf{q}$  is the position of the particle not on the periodic torus but in an unbounded domain obtained by periodically replicating the fixed unit cell. In our tests the particles are localized to a single unit cell and do not interact with periodic image particles; in more general situations such as sheared suspensions more complicated approaches (reminiscent of Lees-Edwards boundary conditions commonly employed in molecular dynamics) are necessary to account for the

domain width, $L$	$64h$
hydrodynamic radius, $a$	$1.04h$
spring constant, $k$	$1(k_B T/h^2)$
time step size $\frac{\Delta t}{\tau}$	0.22, 0.11, 0.02
diffusive CFL number $\beta$	0.45, 0.22, 0.05
Weissenberg number	1.0

Table III: Parameters for the simulation of a single particle in shear flow.

domain width, $L$	$32h$
well separation, $b$	$5h$
hydrodynamic radius, $a$	$1.25h$
spring constant, $k$	$10(k_B T/h^2)$
time step size $\frac{\Delta t}{\tau}$	0.3, 0.08
diffusive CFL number $\beta$	0.06, 0.015
Weissenberg number	1.0

Table IV: Parameters for the simulation of two particles in shear flow.

lack of periodicity in shear flow [87]. Alternatively, one can use periodic flows of the form  $u_x \sim \sin ky$  with  $k$  sufficiently small (i.e., periodic box sufficiently large) to approach the limit  $k \rightarrow 0$ .

### 1. A Single Particle

In this simulation, a single particle is placed in a background shear flow and is attached to an anchor location,  $\mathbf{q}_0$ , by a harmonic spring with potential  $U = (k/2) \|\mathbf{q} - \mathbf{q}_0\|^2$ . The strength of the shear flow relative to the harmonic force is measured with the dimensionless Weissenberg number,  $Wi = \dot{\gamma}\tau$ , where  $\tau = (\mu k)^{-1}$  is the timescale of the particle's relaxation to its anchor location due to the harmonic spring. Theoretical results are given for three dimensions in Ref. [85], but the analysis also holds in two dimensions with the appropriate diffusion coefficient. We perform the single-particle tests in two dimensions and the two-particle tests in three dimensions.

The simulation parameters are given in Table III. The strength of the spring is such that the equilibrium Gaussian distribution for  $\|\mathbf{q} - \mathbf{q}_0\|$  has a standard deviation of  $h$  (one grid cell). We define the fluctuation  $\tilde{x} = x - \langle x \rangle$ , where  $\langle x \rangle$  is the average position, and similarly for  $y$ . The time correlations  $C_{xx}(t) = \langle \tilde{x}(t)\tilde{x}(0) \rangle$ ,  $C_{yy}(t) = \langle \tilde{y}(t)\tilde{y}(0) \rangle$ , and  $C_{xy}(t) = \langle \tilde{x}(t)\tilde{y}(0) \rangle$  are then calculated and compared to the known theoretical results [85],

$$\begin{aligned}\hat{C}_{xx}(t) &:= \frac{k_B T}{k} \left[ 1 + \frac{Wi^2}{2} \left( 1 + \frac{|t|}{\tau} \right) \right] e^{-|t|/\tau} \\ \hat{C}_{xy}(t) &:= \frac{k_B T}{k} \frac{Wi}{2} \left( 1 + 2\frac{t}{\tau} H(t) \right) e^{-t/\tau},\end{aligned}$$

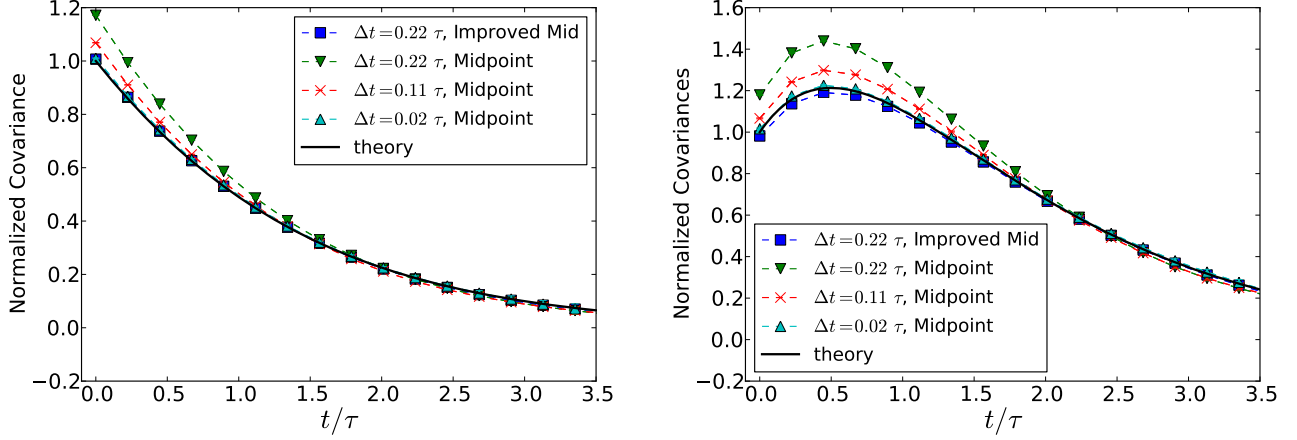


Figure 6: Normalized time correlation functions for a single particle in a harmonic potential in the presence of shear flow. As the time step size is reduced, the numerical results converge to the theoretical expressions, substantially faster for the improved midpoint algorithm. Error bars of two standard deviations are drawn, and are generally on the order of symbol size. (Left panel) Autocorrelation of the displacement of the particle in the direction of flow,  $\langle \tilde{x}(t)\tilde{x}(0) \rangle$ . (Right panel) Cross correlation of the displacements in flow and shear directions,  $\langle \tilde{x}(t)\tilde{y}(0) \rangle$ .

where  $H(t)$  is the Heaviside function. The time correlations in the direction of shear,  $C_{yy}(t)$ , are not influenced by the background flow and are omitted. It can be seen in Fig. 6 that the simulation results converge to the correct time correlations as the time step size is reduced, which confirms that the FIB method accurately captures the dynamics of an immersed particle subject to external forcing and flow.

Significantly more accurate time correlation functions can be obtained by using the improved midpoint scheme (38). Because the equations of motion of a single blob in shear flow are additive-noise equations, the improved midpoint scheme is second-order accurate. This is confirmed in Fig. 6 where we see that the second-order scheme is able to obtain the same accuracy as the first-order scheme with a time step that is an order of magnitude larger.

## 2. Two Particles

In the previous section, we tested the ability of our algorithm to reproduce the dynamics of a single particle. We now test the ability of our approach also correctly capture the hydrodynamic interactions between particles. We extend the previous simulation to include two particles, each in its own harmonic potential with minima separated by vector of length  $b$  in the direction of flow,  $U(\mathbf{q}) = (k/2) \|\mathbf{q} - \mathbf{q}_{\min}\|^2$ , where  $\mathbf{q}_{\min}$  are the positions of the minima of the two harmonic wells. The shear flow used is the same as in the previous section. In this simulation we study the correlations between the motion of particle 1 and particle 2 (cross-correlations), as well as correlations of particle 1 with itself (self-correlations).

The self-correlations are different from the single-particle case due to the disturbances in the fluid caused by the presence of the second particle.

Theoretical results are calculated in Ref. [86] for an infinite domain by linearizing the equations around the equilibrium location of the particles  $\bar{\mathbf{q}}$  (which is in general different from  $\mathbf{q}_{\min}$ ) and forming equations of motion for the fluctuations  $\tilde{\mathbf{q}} = \mathbf{q} - \bar{\mathbf{q}}$  under the assumption that  $\tilde{\mathbf{q}}$  is small. This leads to a simple Ornstein-Uhlenbeck process [86]

$$\frac{d\tilde{\mathbf{q}}}{dt} = \mathbf{A}\tilde{\mathbf{q}} - k\mathcal{M}(\bar{\mathbf{q}})\tilde{\mathbf{q}} + \mathbf{B}\tilde{\mathbf{q}} + \mathcal{M}^{\frac{1}{2}}(\bar{\mathbf{q}})\mathcal{W}(t), \quad (48)$$

where  $\mathbf{A}$  is the shear rate tensor,  $A_{12} = A_{45} = \dot{\gamma}$  and all other entries are zero, and  $\mathbf{B}_{ij} = \partial_j \mathcal{M}_{ik}(\bar{\mathbf{q}}) (\mathbf{q}_{\min}^{(k)} - \bar{\mathbf{q}}^{(k)})$ . Because we have chosen to have the shear flow in the direction that separates the wells, we have that  $\bar{\mathbf{q}} = \mathbf{q}_{\min}$  if we choose  $\bar{\mathbf{q}}_1^{(2)} = \bar{\mathbf{q}}_2^{(2)} = 0$ , and therefore  $\mathbf{B} = \mathbf{0}$  and no derivatives of the mobility are required. Since we employ periodic boundary conditions for the velocity in our simulations, we approximate  $\mathcal{M}(\bar{\mathbf{q}})$  using a periodic correction to the Rotne-Prager-Yamakawa tensor calculated with an Ewald sum [88] and evaluated at position  $\bar{\mathbf{q}}$ .

The simulation was run using a periodic three dimensional domain, and the temperature was set such that the standard deviation of the particles' displacements was  $\sqrt{10}h$ , keeping the particles near the potential minima and thus giving better agreement with the linearized theoretical calculations. The simulation parameters are given in Table IV. The numerical time correlation functions shown in Figs. 7, 8 and 9 are in good agreement with the theoretical results for the moderate time step

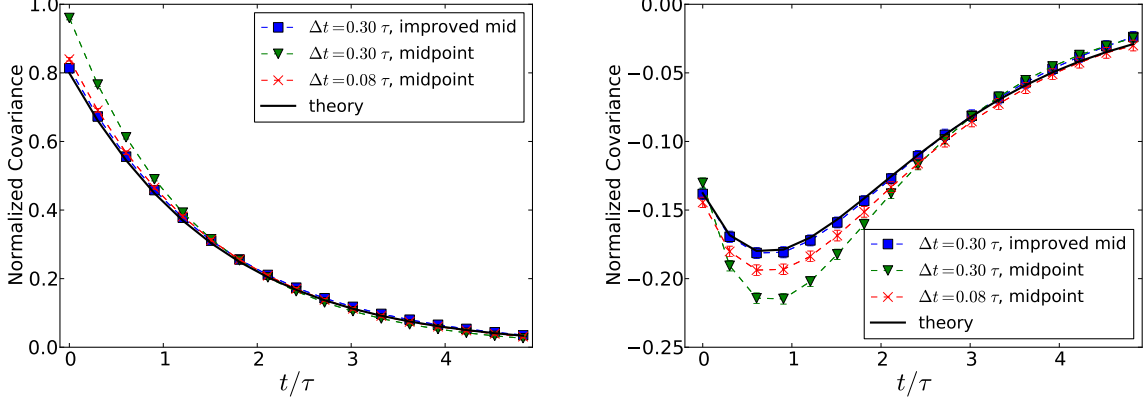


Figure 7: Time correlation functions for two particles bound by harmonic potentials in the presence of shear flow. (*Left panel*) Autocorrelation of the displacement of one of the particles in the direction of flow,  $\langle \tilde{x}_1(t) \tilde{x}_1(0) \rangle$ . (*Right panel*) Correlation of the displacements of the two particles in the direction of flow,  $\langle \tilde{x}_1(t) \tilde{x}_2(0) \rangle$ .

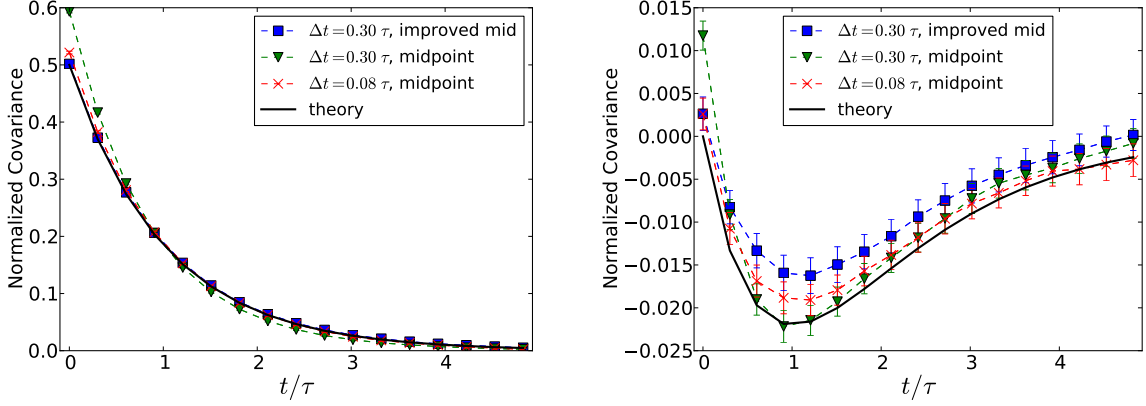


Figure 8: (*Left panel*) Autocorrelation of the displacement of one of the particles in the direction of shear  $\langle \tilde{y}_1(t) \tilde{y}_1(0) \rangle$ . (*Right panel*) Correlation of the displacements of the two particles in the direction of the shear,  $\langle \tilde{y}_1(t) \tilde{y}_2(0) \rangle$ .

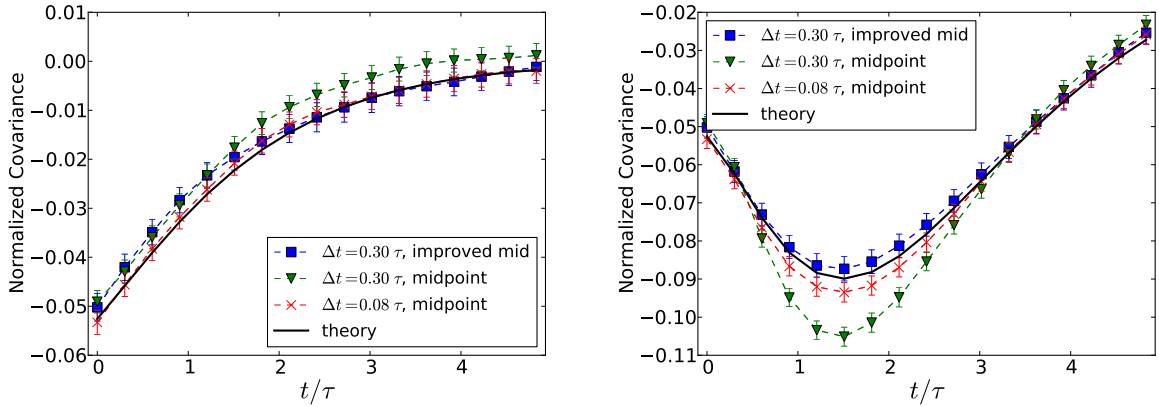


Figure 9: Cross correlation of the displacements of the two particles in the shear and flow directions,  $\langle \tilde{y}_2(t) \tilde{x}_1(0) \rangle$  (left panel) and  $\langle \tilde{x}_1(t) \tilde{y}_2(0) \rangle = \langle \tilde{y}_2(-t) \tilde{x}_1(0) \rangle$  (right panel).

size. The error is improved as the time step size is decreased to better resolve the relevant timescale. Note that the improved midpoint scheme (38) gives better agreement with theoretical results, as it is second-order accurate for this example because the equations of motion are essentially linear. Note that a visible mismatch with the theoretical curve is seen for the cross-correlation  $\langle \tilde{y}_1(t)\tilde{y}_2(0) \rangle$  in the right panel of Fig. 8; since the two midpoint schemes are in agreement with each other this mismatch comes from the approximations made in the theory.

### E. Colloidal Gelation

In this section, we confirm that the FIB method correctly reproduces the dynamical effect of multi-particle hydrodynamic interactions for a collection of colloidal particles interacting via excluded-volume (non-bonded) interactions with an attractive tail. It has been demonstrated that hydrodynamic interactions play a significant role in the process of colloidal gelation [89]. Here we use the FIB method to study a model test example of colloidal cluster dynamics, and compare the FIB results to those of traditional Brownian Dynamics (with hydrodynamic interactions).

As a simple test problem illustrating the effect of hydrodynamics on gelation, a 13-particle colloidal cluster collapse example has been constructed in Ref. [89]. The physical system consists of 13 blobs initially placed at the vertices of an icosahedron (see Fig. 4 in Ref. [89]), and then released to relax toward the thermodynamically-preferred collapsed (bound) cluster of 13 spheres. In the absence of hydrodynamic interactions the collapse is rapid. In the presence of hydrodynamic interactions, however, the cluster undergoes a slow rearrangement process through multiple elongated configurations (see Fig. 4 in Ref. [89]) before it collapses. This results in a dramatic slowing down of the collapse when hydrodynamics is accounted for.

The collapse of the cluster can be monitored via the radius of gyration of the cluster  $R_g(t)$ . An ensemble average  $\langle R_g(t) \rangle$  over 64 trajectories obtained using the FIB method is shown in Fig. 10. In the first set of simulations, we employ periodic boundary conditions with a grid of  $32^3$  cells and use the GPU-based code *fluam* with the three-point Peskin kernel [19] and the simple midpoint integrator. The second set of simulations were performed using IBAMR on a periodic grid of  $64^3$  cells with the four-point kernel and the improved midpoint integrator. We use the Asakura-Oosawa depletion force with a repulsive Lennard-Jones interaction, following Ref. [89]. Important parameters of our simulations are summarized in Table V.

It is important to note that the time step size used for these simulations is much smaller than the Brownian time scale  $\tau_B = a^2/\chi \approx 50$ . This is because the time step size here is severely limited by stability considerations.

grid spacing $\Delta x$	3.27
grid size	$32^3$
shear viscosity $\eta$	1
time step size $\Delta t$	0.05 (simple) or 0.1 (improved)
temperature $k_B T$	12.3
LJ strength $\epsilon$	10
LJ / hydro diameter $\sigma$	6.4
number of particles $N$	13

Table V: Parameters used in the colloidal cluster collapse simulations shown in the right panel of Fig. 5. These are chosen to match those in Ref. [89] as closely as possible.

The stiff hard-core repulsion between the particles and the fact that the particles are close to each other due to the attractive tail combine to make the simple midpoint scheme unstable for  $\Delta t > 0.05$  (determined empirically). The improved midpoint scheme shows slightly improved stability and we have successfully used it for  $\Delta t = 0.1$ , however, the cost per time step is approximately doubled so this improvement is not substantial. Achieving larger time step sizes and avoiding exploding (unstable) trajectories requires specialized temporal integration methods such as Metropolization[103] [90]. Note that in a small fraction of the trajectories (we only observed two such trajectories) the cluster dissolves instead of collapsing. This could be the signature of a rare event but it could also be an artifact of numerical instabilities arising from the stiff interparticle potentials; lacking better statistics we have excluded these trajectories from the averages.

In Ref. [89], the authors compare their method to BD without hydrodynamic interactions (HI) (i.e., employ a mobility that is a diagonal matrix), but do not compare to BD with hydrodynamic interactions. In the right panel of Fig. 10 we compare the results from the FIB method to BD with and without HI. We included hydrodynamics using the free-space Rotne-Prager-Yamakawa (RPY) mobility (7), and employed a simple Euler-Maruyama integrator with time step size  $\Delta t = 0.05$  instead of the Fixman method since the divergence of the free-space RPY mobility vanishes identically. The results in Fig. 10 demonstrate that both BD-with HI and the FIB method reproduce the slowing down (relative to BD without HI) in the cluster collapse and agree with each other. While inclusion of higher-order effects such as stresslets and lubrication, may lead to some quantitative differences, our results are already in good agreement with those in Fig. 4 in Ref. [89] and indicate that the primary effect comes from the far-field hydrodynamic interactions.

## VI. CONCLUSIONS

We have developed a method for performing Brownian Dynamics (BD) with hydrodynamic interactions in confined geometries such as slit or square channels or cham-

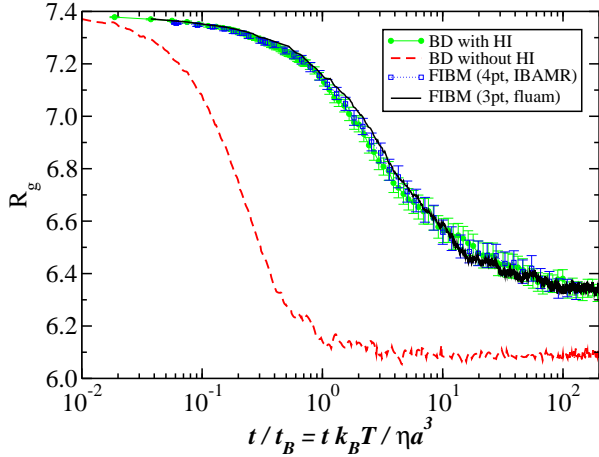


Figure 10: Relaxation of the radius of gyration of a colloidal cluster of 13 spheres toward equilibrium, as obtained by averaging 64 independent simulations. The FIB method is compared to traditional Brownian Dynamics (BD) with and without hydrodynamic interactions (HI). For comparison, FIB simulations were performed both using the *fluam* code with the three-point kernel and a domain of  $32^3$  grid cells, as well as using the IBAMR code with the four-point kernel and  $64^3$  grid cells.

bers. Unlike traditional methods for BD, our FIB method does not rely on analytical Green’s functions, and only requires the numerical solution of a single steady Stokes system per time step to capture both the deterministic, stochastic, and thermal drift contributions to the overdamped dynamics of the hydrodynamically-coupled particles. The FIB method is particularly appealing when dealing with more complex boundary conditions such as confined flows in non-trivial channel geometries, since analytical solutions are quite involved and ensuring a positive semi-definite mobility is nontrivial, even in the presence of only a single no-slip planar wall [15, 32]. Computing analytical solutions in cases where there are osmophoretic flows at the boundaries, as in active suspensions of particles [48], is essentially impossible because the boundary condition itself comes from the solution of another nontrivial reaction-diffusion problem. The only alternative would be to use relatively-expensive and complex boundary integral methods [91–93], none of which, to our knowledge, include the effects of thermal fluctuations.

Following the completion of this work we learned about a related recent extension of the SELM approach to use a (P1-MINI) finite-element Stokes solver to generate the hydrodynamic response [55], very similar to the approach we independently took in this work. Note, however, that our temporal integrators are different from the Euler-Maruyama scheme used in Ref. [55], which requires calculating the divergence of the mobility by other means (We remark that the issue of computing the divergence

of the mobility does not appear to be addressed directly in Ref. [55].). In terms of spatial discretizations, the key relation  $-\mathcal{L}^{-1}\mathbf{L}\mathcal{L}^{-1} = \mathcal{L}^{-1}$  is used in both works to generate the correct stochastic increments by simply solving the saddle-point steady Stokes problem. A key difference, however, is that on the structured MAC grid used in this work the generation of a stochastic stress tensor with covariance  $\sim -\mathbf{L}$  is straightforward [69], where as accomplishing the same for unstructured FEM grids appears to require an iterative stochastic multigrid method [55]. Furthermore, the P1-MINI discretization is only first-order spatially accurate and requires more degrees of freedom (DOF) per cell, where as the structured staggered (MAC) grid (which can be thought of as a particular FEM discretization) achieves second-order spatial accuracy with only a single velocity DOF per grid face and a single pressure DOF per cell center. This makes the methods developed here particularly attractive, due to their simplicity and efficiency, in simple confined geometries such as channels or chambers. At the same time, unstructured FEM discretizations have a notable advantage for complex geometries. Additionally, achieving variable spatial resolution is natural on unstructured grids [55] but requires (block structured) adaptive mesh refinement (AMR) techniques [77] on structured grids. Adaptive resolution is very important at low densities of suspended particles to avoid using a fine spatial grid to resolve long-ranged hydrodynamics; this is in fact a key advantage of using Green’s functions instead of numerical solvers. In future work we will consider solving the fluctuating Stokes equations on block-structured refined staggered grids.

The FIB method presented here and related methods [20, 55] are only a first step toward the ultimate goal of performing Brownian (i.e., overdamped) dynamics for a collection of rigid and flexible bodies in flow in the presence of complex boundaries. Achieving that goal may ultimately require a combination of techniques, such as multipole series, immersed boundary [94] and immersed finite-element [18], or boundary integral representations for the suspended structures, together with cut cell (embedded boundary) or finite-element methods [55] for representing the complex geometry. What our work makes evident is that thermal fluctuations are most easily and consistently included by using fluctuating hydrodynamics combined with appropriate multiscale temporal integrators. This illustrates the power of a bottom-up approach in which one starts with the fundamental formulation of the fluid dynamics of suspensions [41–43] and then coarse-grains in space and time to reach larger length scales and longer time scales, instead of starting at the top from a formulation of the equations of motion that contains difficult-to-calculate objects such as multi-body mobility or resistance tensors that hide all of the coarse-grained information inside them.

## Acknowledgments

We thank Eric Vanden-Eijnden and Anthony Ladd for informative discussions, and Ranojoy Adhikari and Eric Keaveny for helpful comments on the manuscript. S. Delong was supported by the DOE office of Advanced Scientific Computing Research under grant DE-FG02-88ER25053. A. Donev was supported in part by the Air Force Office of Scientific Research under grant number FA9550-12-1-0356. B. Griffith acknowledges research support from the National Science Foundation under awards OCI 1047734 and DMS 1016554. R. Delgado-Buscalioni and F. Balboa acknowledge funding from the Spanish government FIS2010-22047-C05 and from the Comunidad de Madrid MODELICO-CM (S2009/ESP-1691). Collaboration between A. Donev and R. Delgado-Buscalioni was fostered at the Kavli Institute for Theoretical Physics in Santa Barbara, California, and supported in part by the National Science Foundation under Grant No. NSF PHY05-51164.

## Appendix

### Appendix A: Weak Temporal Accuracy

In this Appendix we show that the algorithms outlined in Section IV are first order weakly accurate temporal integrators for the system (18). It suffices to show that the

first three moments of the numerical one-step increment in time match to first order the moments of the exact increment [95]. Without loss of generality, we consider the case  $\eta = 1$  for this analysis. The RFD term (37) introduces an error proportional to  $\delta^2$ . This is a spatial truncation error and will be ignored in the context of temporal accuracy. Note that in practice,  $\delta$  will be a very small fixed value that introduces a negligible truncation error to the approximation of the thermal drift.

For the continuous equation, we have, to first order,

$$\begin{aligned}\Delta_\alpha^q &\equiv q_\alpha((n+1)\Delta t) - q_\alpha(n\Delta t) \\ &= \Delta t (\mathcal{J}_{\alpha\mu}^n \mathcal{L}_{\mu\nu}^{-1} \mathcal{S}_{\nu\beta}^n F_\beta^n \\ &\quad + \sqrt{2k_B T} \int_{t'}^t \mathcal{J}_{\alpha\mu}^n \mathcal{L}_{\mu\nu}^{-1} \tilde{D}_{\nu\beta} dW_\beta \\ &\quad + \Delta t k_B T \partial_\gamma \cdot (\mathcal{J}_{\alpha\mu}^n \mathcal{L}_{\mu\nu}^{-1} \mathcal{S}_{\nu\gamma}^n) + O(\Delta t^{\frac{3}{2}}),\end{aligned}\tag{A1}$$

where  $\mathcal{J}$ ,  $\mathcal{S}$  and  $F$  are evaluated at the beginning of the time step. The first moment of the true increment is

$$\begin{aligned}E[\Delta_\alpha^q] &\equiv \Delta t \mathcal{J}_{\alpha\mu}^n \mathcal{L}_{\mu\nu}^{-1} \mathcal{S}_{\nu\beta}^n F_\beta^n + O(\Delta t^2) \\ &\quad + \Delta t k_B T \left[ \mathcal{J}_{\alpha\mu}^n \mathcal{L}_{\mu\nu}^{-1} \partial_\gamma (\mathcal{S}_{\nu\gamma}^n) + \partial_\gamma (\mathcal{J}_{\alpha\mu}^n) \mathcal{L}_{\mu\nu}^{-1} \mathcal{S}_{\nu\gamma}^n \right].\end{aligned}$$

#### 1. First Order Midpoint Scheme

Looking at the discrete increment to first order, we get,

$$\begin{aligned}\bar{\Delta}_\alpha^q &\equiv q_\alpha^{n+1} - q_\alpha^n = \Delta t \mathcal{J}_{\alpha\mu}^n \mathcal{L}_{\mu\nu}^{-1} \mathcal{S}_{\nu\beta}^n F_\beta^n \\ &\quad + \Delta t \mathcal{J}_{\alpha\mu}^n \mathcal{L}_{\mu\nu}^{-1} \frac{k_B T}{\delta} [\mathcal{S}_{\nu\beta}^n (q^n + \frac{\delta}{2} \tilde{W}^n) \tilde{W}_\beta^n - \mathcal{S}_{\nu\beta}^n (q^n - \frac{\delta}{2} \tilde{W}^n) \tilde{W}_\beta^n] \\ &\quad + (\Delta t)^{\frac{1}{2}} \left( \frac{k_B T}{2\Delta V} \right)^{\frac{1}{2}} \partial_\gamma (\mathcal{J}_{\alpha\mu}^n) (q_\gamma^{n+\frac{1}{2}} - q_\gamma^n) \mathcal{L}_{\mu\nu}^{-1} \tilde{D}_{\nu\beta} W_\beta^n \\ &\quad + \sqrt{\frac{2k_B T \Delta t}{\Delta V}} \mathcal{J}_{\alpha\mu}^n \mathcal{L}_{\mu\nu}^{-1} \tilde{D}_{\nu\beta} W_\beta^n + O(\Delta t^{\frac{3}{2}}).\end{aligned}$$

Inserting the expression for the predictor increment  $q^{n+\frac{1}{2}} - q^n$ , simplifying and ignoring terms of order  $\Delta t^2$ , along with terms of order  $\Delta t^{\frac{3}{2}}$  with zero expectation, and terms of order  $\delta^2$ , we obtain

$$\begin{aligned}\bar{\Delta}_\alpha^q &= \Delta t \mathcal{J}_{\alpha\mu}^n \mathcal{L}_{\mu\nu}^{-1} \mathcal{S}_{\nu\beta}^n F_\beta^n \\ &\quad + \Delta t k_B T \mathcal{J}_{\alpha\mu}^n \mathcal{L}_{\mu\nu}^{-1} \partial_\gamma (\mathcal{S}_{\nu\beta}^n) \tilde{W}_\gamma^n \tilde{W}_\beta^n \\ &\quad + \frac{\Delta t k_B T}{\Delta V} \partial_\gamma (\mathcal{J}_{\alpha\mu}^n) (\mathcal{J}_{\gamma\epsilon}^n \mathcal{L}_{\epsilon\zeta}^{-1} \tilde{D}_{\zeta\eta} W_\eta^n) \mathcal{L}_{\mu\nu}^{-1} \tilde{D}_{\nu\beta} W_\beta^n \\ &\quad + \sqrt{\frac{2k_B T \Delta t}{\Delta V}} \mathcal{J}_{\alpha\mu}^n \mathcal{L}_{\mu\nu}^{-1} \tilde{D}_{\nu\beta} W_\beta^n + O(\Delta t^{\frac{3}{2}}).\end{aligned}$$

The first moment of this increment is obtained by using the adjoint relation  $\mathcal{J}_{\gamma\epsilon} = \mathcal{S}_{\epsilon\gamma} \Delta V$ , as well as  $\mathcal{L}_{\epsilon\zeta}^{-1} \tilde{D}_{\zeta\eta} \mathcal{L}_{\mu\nu}^{-1} \tilde{D}_{\nu\beta} \langle W_\eta^n W_\beta^n \rangle = \mathcal{L}_{\epsilon\zeta}^{-1} \tilde{D}_{\zeta\eta} \tilde{D}_{\nu\eta} \mathcal{L}_{\mu\nu}^{-1} = \mathcal{L}_{\mu\epsilon}^{-1}$  by virtue of (20),

$$\begin{aligned}E[\bar{\Delta}_\alpha^q] &= \Delta t \mathcal{J}_{\alpha\mu}^n \mathcal{L}_{\mu\nu}^{-1} \mathcal{S}_{\nu\beta}^n F_\beta^n + O(\Delta t^2) \\ &\quad + \Delta t k_B T \left[ \mathcal{J}_{\alpha\mu}^n \mathcal{L}_{\mu\nu}^{-1} \partial_\gamma (\mathcal{S}_{\nu\gamma}^n) + \partial_\gamma (\mathcal{J}_{\alpha\mu}^n) \mathcal{L}_{\mu\epsilon}^{-1} \mathcal{S}_{\epsilon\gamma}^n \right],\end{aligned}$$

which matches the  $O(\Delta t)$  terms in the continuous increment (A1).

The second moment of the discrete increment,

$$E[\bar{\Delta}_\alpha^q \bar{\Delta}_\eta^q] = 2\Delta t k_B T \mathcal{J}_{\alpha\mu} \mathcal{L}_{\mu\nu}^{-1} \mathcal{S}_{\nu\eta} + O(\Delta t^2),$$

also matches the continuous second moment to second order. Finally the third moments are both  $O(\Delta t^2)$ , because the order  $\Delta t^{\frac{3}{2}}$  terms are mean zero.

## 2. Improved Midpoint Scheme

We show here that the scheme given by Eq. (38) is also first order weakly accurate. The discrete increment for this scheme to first order is

$$\begin{aligned} \bar{\Delta}_\alpha^q &\equiv q_\alpha^{n+1} - q_\alpha^n = \Delta t \mathcal{J}_{\alpha\mu} \mathcal{L}_{\mu\nu}^{-1} \left[ \mathcal{S}_{\nu\beta}^n F_\beta^n + \sqrt{\frac{k_B T}{\Delta V \Delta t}} \tilde{D}_{\nu\beta} (W_\beta^{n,1} + W_\beta^{n,2}) \right] \\ &+ \sqrt{\frac{\Delta t k_B T}{\Delta V}} \partial_\eta (\mathcal{J}_{\alpha\mu}^n) \left( q_\eta^{n+\frac{1}{2}} - q_\eta^n \right) \mathcal{L}_{\mu\nu}^{-1} \tilde{D}_{\nu\beta} (W_\beta^{n,1} + W_\beta^{n,2}) \\ &+ \frac{\Delta t k_B T}{\delta} \mathcal{J}_{\alpha\mu} \mathcal{L}_{\mu\nu}^{-1} \left[ \mathcal{S}_{\nu\beta}(\mathbf{q}^n + \frac{\delta}{2} \tilde{\mathbf{W}}^n) \tilde{W}_\beta^n - \mathcal{S}_{\nu\beta}(\mathbf{q}^n - \frac{\delta}{2} \tilde{\mathbf{W}}^n) \tilde{W}_\beta^n \right] + O(\Delta t^{\frac{3}{2}}). \end{aligned}$$

Inserting the expression for the predictor increment and removing terms that are either  $O(\Delta t^2)$ ,  $O(\Delta t^{\frac{3}{2}})$  with

mean zero, or  $O(\delta^2)$ , we get,

$$\begin{aligned} \bar{\Delta}_\alpha^q &= \Delta t \mathcal{J}_{\alpha\mu} \mathcal{L}_{\mu\nu}^{-1} \mathcal{S}_{\nu\beta}^n F_\beta^n \\ &+ \frac{\Delta t k_B T}{\Delta V} \partial_\eta (\mathcal{J}_{\alpha\mu}^n) \left( \mathcal{J}_{\eta\kappa}^n \mathcal{L}_{\kappa\rho}^{-1} \tilde{D}_{\rho\zeta} W_\zeta^{n,1} \right) \mathcal{L}_{\mu\nu}^{-1} \tilde{D}_{\nu\beta} (W_\beta^{n,1} + W_\beta^{n,2}) \\ &+ \Delta t k_B T \mathcal{J}_{\alpha\mu} \mathcal{L}_{\mu\nu}^{-1} \partial_\beta (\mathcal{S}_{\nu\beta}^n) \\ &+ \sqrt{\frac{\Delta t k_B T}{\Delta V}} \mathcal{J}_{\alpha\mu} \mathcal{L}_{\mu\nu}^{-1} \tilde{D}_{\nu\beta} (W_\beta^{n,1} + W_\beta^{n,2}) + O(\Delta t^{\frac{3}{2}}). \end{aligned}$$

The second and third terms on the right hand side of this expression give us the thermal drift. The first moment is identical to that of the simple scheme to  $O(\Delta t)$ , as is the second moment. The third moments of both the discrete and continuous terms are already each  $O(\Delta t^2)$ . Note that for the special case of additive noise, such as for example the linearized equation (48), the improved midpoint scheme can be shown to match the first five moments of the true increment to  $O(\Delta t^2)$ , and is thus weakly second-order accurate (see Appendix A1 in Ref. [68]).

## Appendix B: Including Stresslet Terms

As summarized in Section II C and discussed at length in the work of Maxey and collaborators [51, 52, 62], the simple coupling between the fluid and the particles used here correctly reproduces the hydrodynamic interactions between particles only up to the Rotne-Prager level (including in the presence of boundaries). This is because

only the *monopole* term (*Stokeslet*) is included in the fluid-particle force, along with the Faxen correction for the resulting particle velocity. As a consequence the present approach can only accurately resolve the fluid flow at distances larger than the typical size of the particles. For traditional applications of Brownian Dynamics such as polymeric fluids [26, 27, 29, 96] this is probably sufficient, since polymer chains are themselves described at a coarse-grained level and in reality they are not made of a collection of rigid spheres linked with spheres or rods. For colloidal suspensions, however, at higher packing densities one must include higher-order multipole terms in order to more accurately capture the hydrodynamics, as done in the method of Stokesian Dynamics [31] and the improved Force Coupling Method (FCM) [51]. This amounts to including the anti-symmetric component of the dipole (*rotlet*) and the symmetric components of the dipole (*stresslet*) force terms. Note that here we do not discuss lubrication forces.

It is not difficult to extend our approach to also include the rotlet contributions, as has been done by Keaveny



[20] in the fluctuating FCM method. Firstly, particle rotational degrees of freedom would need to be added to the blob description, along with an angular velocity  $\boldsymbol{\omega}_i$  for each blob. We would need to impose an additional *rotational no-slip* constraint, requiring that the particle rotate with the locally-averaged angular velocity of the fluid,  $\boldsymbol{\omega} = \boldsymbol{\mathcal{J}}(\nabla \times \mathbf{v})/2$ , and distribute (spread) the torque  $\boldsymbol{\tau}$  applied on the particles as a torque density  $\mathbf{f}_\tau = \nabla \times (\boldsymbol{\mathcal{S}}\boldsymbol{\tau})/2$  in the fluid momentum equation. This type of approach has already been employed in deterministic immersed-boundary methods to model suspensions of neutrally-buoyant semi-rigid rods [97, 98]. The FIB method and the discrete fluctuation-dissipation results we presented continue to apply since inclusion of rotation simply amounts to augmenting the local averaging and spreading operators. The main difficulties are in developing a translationally-invariant and accurate discretization for the curl operator and its adjoint therot operator, including in the presence of boundaries.

Inclusion of the stresslet contributions, on the other hand, is not trivial as it requires including an additional *rigidity constraint* on the locally-averaged deformation tensor, as proposed by Maxey and collaborators in the context of the deterministic FCM [51] and extended to account for thermal fluctuations by Keaveny [20]. In this appendix we present the continuum formulation including stresslets, and demonstrate that the random increments can easily be generated by including the random stress in the Stokes equations. This has already been observed and proven by Keaveny in the Appendices of Ref. [20]; here we present a simple proof using compact operator notation [17]. Importantly, we do not rely on periodic boundary conditions and Fourier transform techniques, thus demonstrating that the power of the fluctuating hydrodynamics approach to modeling Brownian motion in confined suspensions.

We will omit rotlet contributions here by focusing on the case when there are no torques applied on the particles and assuming that the particles are spherical, so that their orientation does not affect the external or inter-particle forces. We can account for the rigidity of the particle by including a constraint that the locally the rate of strain of the fluid velocity vanish inside the particle, approximated here in a spirit similar to the no-slip constraint (13) [51],

$$\int \delta_b(\mathbf{q}_i - \mathbf{r}) \left[ \nabla \mathbf{v}(\mathbf{r}, t) + \nabla^T \mathbf{v}(\mathbf{r}, t) \right] d\mathbf{r} \equiv (\boldsymbol{\mathcal{K}}\mathbf{v})_i = 0. \quad (\text{B1})$$

Here  $\boldsymbol{\mathcal{K}}(\mathbf{q})$  is linear integro-differential operator that locally-averages the strain rate. In principle a different kernel  $\delta_b \neq \delta_a$  can be used here in order to better approximate the behavior of a rigid sphere [51]. In the discrete setting one would have to construct a discrete operator (matrix)  $\boldsymbol{\mathcal{K}}$  that gives good translational invariance; this is a nontrivial task that amounts to constructing an immersed boundary representation of force dipoles similar to that for monopoles constructed by Peskin [54]. Enforcing the constraint (B1) requires including Lagrange mul-

tipliers (stresslets)  $\boldsymbol{\Lambda}_i$  in the velocity equation (9) [51],  $\nabla \cdot \mathbf{v} = 0$  and

$$\begin{aligned} \rho \partial_t \mathbf{v} + \nabla \pi &= \eta \nabla^2 \mathbf{v} + \sqrt{2\eta k_B T} \nabla \cdot \boldsymbol{\mathcal{Z}} + \mathbf{f}_{\text{th}} \\ &+ \sum_i \mathbf{F}_i \delta_a(\mathbf{q}_i - \mathbf{r}) + \sum_i \boldsymbol{\Lambda}_i \nabla \delta_b(\mathbf{q}_i - \mathbf{r}), \end{aligned} \quad (\text{B2})$$

where the unknown stresslets  $\boldsymbol{\Lambda}_i$  are symmetric traceless  $d \times d$  tensors that need to be solved for.

Putting the pieces together and using compact composite operator notation we can write the equations of motion including stresslet terms in a form that applies either to the continuum or the spatially-discretized equations,

$$\begin{aligned} \rho \partial_t \mathbf{v} &= \eta \mathbf{L} \mathbf{v} + \mathbf{D}^* \pi + \boldsymbol{\mathcal{K}}^* \boldsymbol{\Lambda} + \mathbf{f} \\ \mathbf{D} \mathbf{v} &= 0 \\ \boldsymbol{\mathcal{K}} \mathbf{v} &= \mathbf{0} \end{aligned} \quad (\text{B3})$$

where  $\boldsymbol{\Lambda} = \{\boldsymbol{\Lambda}_1, \dots, \boldsymbol{\Lambda}_N\}$  are unknown stresslets and

$$\mathbf{f} = \boldsymbol{\mathcal{J}}^* \mathbf{F} + \sqrt{\eta k_B T} \tilde{\mathbf{D}} \mathbf{W} + \mathbf{f}_{\text{th}}. \quad (\text{B4})$$

The (translational) dynamics of the particles continues to be described by the no-slip condition  $d\mathbf{q}/dt = \boldsymbol{\mathcal{J}}\mathbf{v}$ . It is evident from the form of (B3) that the rigidity constraint  $\boldsymbol{\mathcal{K}}\mathbf{v} = \mathbf{0}$  is in principle no different from the divergence-free constraint, except for the fact that  $\boldsymbol{\mathcal{K}}(\mathbf{q})$  depends on the configuration of the particles just like  $\boldsymbol{\mathcal{J}}(\mathbf{q})$  does. In fact, as observed by Keaveny [20] and also used in Stokesian Dynamics, the inclusion of stresslets simply amounts to redefining the mobility matrix, and the overdamped limiting dynamics for the positions of the particles is still given by (3). Equation (3) in fact applies much more generally and is not specific to multipole expansions.

The form of the modified mobility matrix can be obtained by deleting the inertial term  $\rho \partial_t \mathbf{v}$  and solving the augmented steady Stokes system (B3) using a Schur complement approach, to obtain

$$\mathbf{v} = \left[ \boldsymbol{\mathcal{L}}^{-1} - \boldsymbol{\mathcal{L}}^{-1} \boldsymbol{\mathcal{K}}^* (\boldsymbol{\mathcal{K}} \boldsymbol{\mathcal{L}}^{-1} \boldsymbol{\mathcal{K}}^*)^{-1} \boldsymbol{\mathcal{K}} \boldsymbol{\mathcal{L}}^{-1} \right] \mathbf{f} = \boldsymbol{\mathcal{N}} \mathbf{f},$$

where  $\boldsymbol{\mathcal{L}}^{-1}$  is the (discrete) inverse Stokes operator given by (29) (note the identical structure of  $\boldsymbol{\mathcal{L}}^{-1}$  and  $\boldsymbol{\mathcal{N}}$ ). This gives the mobility matrix

$$\boldsymbol{\mathcal{M}} = \boldsymbol{\mathcal{J}} \boldsymbol{\mathcal{N}} \boldsymbol{\mathcal{J}}^* = \boldsymbol{\mathcal{J}} \boldsymbol{\mathcal{N}} \mathbf{S}.$$

Just as without stresslets, by solving the steady Stokes equation with the random forcing (B4) one can compute both  $\boldsymbol{\mathcal{M}} \mathbf{F}$  and the stochastic increments. That, is the square root of the mobility matrix can be taken to be  $\boldsymbol{\mathcal{M}}^{\frac{1}{2}} = \boldsymbol{\mathcal{J}} \tilde{\mathbf{D}}$ , as evident from the identity

$$\boldsymbol{\mathcal{J}} \boldsymbol{\mathcal{N}} (\tilde{\mathbf{D}} \tilde{\mathbf{D}}^*) \boldsymbol{\mathcal{N}}^* \boldsymbol{\mathcal{J}}^* = \boldsymbol{\mathcal{J}} \boldsymbol{\mathcal{N}} \mathbf{S} = \boldsymbol{\mathcal{M}},$$

which is the generalization of (31) to account for stresslets.



This shows that, in principle, it is relatively straightforward to incorporate both boundary conditions and stresslets into the FIB algorithm and thus do Stokesian dynamics without Green's functions. In practice, there are significant challenges to surmount to accomplish this goal. The main difficulty is that solving the system (B3) efficiently in the presence of nontrivial boundary conditions is hard and requires the development of novel preconditioners. For periodic domains one can use Fourier

transform techniques to diagonalize the Stokes operator, as used by Keaveny [20], but in general one cannot easily decouple the computation of the stresslets from solving the Stokes system. Furthermore, a nontrivial generalization of the temporal algorithms developed here is required to obtain the correct thermal drift term which comes from the fact that  $\mathcal{N}(\mathbf{q})$  depends on the configuration because  $\mathcal{K}(\mathbf{q})$  does.

- 
- [1] H. Noguchi, N. Kikuchi, and G. Gompper. Particle-based mesoscale hydrodynamic techniques. *Europhysics Letters*, 78:10005, 2007.
  - [2] A. Donev, A. L. Garcia, and B. J. Alder. Stochastic Hard-Sphere Dynamics for Hydrodynamics of Non-Ideal Fluids. *Phys. Rev. Lett.*, 101:075902, 2008.
  - [3] A. Donev, A. L. Garcia, Anton de la Fuente, and J. B. Bell. Diffusive Transport by Thermal Velocity Fluctuations. *Phys. Rev. Lett.*, 106(20):204501, 2011.
  - [4] L.D. Landau and E.M. Lifshitz. *Fluid Mechanics*, volume 6 of *Course of Theoretical Physics*. Pergamon Press, Oxford, England, 1959.
  - [5] J. M. O. De Zarate and J. V. Sengers. *Hydrodynamic fluctuations in fluids and fluid mixtures*. Elsevier Science Ltd, 2006.
  - [6] H. C. Öttinger. *Beyond equilibrium thermodynamics*. Wiley Online Library, 2005.
  - [7] A. Donev, A. L. Garcia, Anton de la Fuente, and J. B. Bell. Enhancement of Diffusive Transport by Nonequilibrium Thermal Fluctuations. *J. of Statistical Mechanics: Theory and Experiment*, 2011:P06014, 2011.
  - [8] B. Z. Shang, N. K. Voulgarakis, and J.-W. Chu. Fluctuating hydrodynamics for multiscale simulation of inhomogeneous fluids: Mapping all-atom molecular dynamics to capillary waves. *J. Chem. Phys.*, 135:044111, 2011.
  - [9] N. K. Voulgarakis and J.-W. Chu. Bridging fluctuating hydrodynamics and molecular dynamics simulations of fluids. *J. Chem. Phys.*, 130(13):134111, 2009.
  - [10] B.Z. Shang, N.K. Voulgarakis, and J.W. Chu. Fluctuating hydrodynamics for multiscale modeling and simulation: Energy and heat transfer in molecular fluids. *J. Chem. Phys.*, 137(4):044117–044117, 2012.
  - [11] A. Donev, A. J. Nonaka, Y. Sun, T. G. Fai, A. L. Garcia, and J. B. Bell. Low Mach Number Fluctuating Hydrodynamics of Diffusively Mixing Fluids. *Communications in Applied Mathematics and Computational Science*, 9(1):47–105, 2014.
  - [12] N. Sharma and N. A. Patankar. Direct numerical simulation of the Brownian motion of particles by using fluctuating hydrodynamic equations. *J. Comput. Phys.*, 201:466–486, 2004.
  - [13] O. B. Usta, A. J. C. Ladd, and J. E. Butler. Lattice-Boltzmann simulations of the dynamics of polymer solutions in periodic and confined geometries. *J. Chem. Phys.*, 122(9):094902, 2005.
  - [14] Anthony JC Ladd, Rahul Kekre, and Jason E Butler. Comparison of the static and dynamic properties of a semiflexible polymer using lattice Boltzmann and Brownian-dynamics simulations. *Physical Review E*, 80(3):036704, 2009.
  - [15] Rahul Kekre, Jason E. Butler, and Anthony J. C. Ladd. Comparison of lattice-Boltzmann and Brownian-dynamics simulations of polymer migration in confined flows. *Phys. Rev. E*, 82:011802, 2010.
  - [16] B. Dünweg and A.J.C. Ladd. Lattice Boltzmann simulations of soft matter systems. *Adv. Comp. Sim. for Soft Matter Sciences III*, pages 89–166, 2009.
  - [17] P. J. Atzberger. Stochastic Eulerian-Lagrangian Methods for Fluid-Structure Interactions with Thermal Fluctuations. *J. Comp. Phys.*, 230:2821–2837, 2011.
  - [18] Adrian M Kopacz, Neelesh A Patankar, and Wing K Liu. The immersed molecular finite element method. *Computer Methods in Applied Mechanics and Engineering*, 233:28–39, 2012.
  - [19] F. Balboa Usabiaga, R. Delgado-Buscalioni, B. E. Griffith, and A. Donev. Inertial Coupling Method for particles in an incompressible fluctuating fluid. *Comput. Methods Appl. Mech. Engrg.*, 269:139–172, 2014. Code available at <https://code.google.com/p/fluum>.
  - [20] Eric E. Keaveny. Fluctuating force-coupling method for simulations of colloidal suspensions. *J. Comp. Phys.*, 269(0):61 – 79, 2014.
  - [21] F. Balboa Usabiaga and R. Delgado-Buscalioni. A minimal model for acoustic forces on Brownian particles. *Phys. Rev. E*, 88:063304, 2013.
  - [22] T. Iwashita, Y. Nakayama, and R. Yamamoto. A Numerical Model for Brownian Particles Fluctuating in Incompressible Fluids. *Journal of the Physical Society of Japan*, 77(7):074007, 2008.
  - [23] Y. Chen, N. Sharma, and N. Patankar. Fluctuating Immersed Material (FIMAT) dynamics for the direct simulation of the Brownian motion of particles. In *IUTAM Symposium on Computational Approaches to Multiphase Flow*, pages 119–129. Springer, 2006.
  - [24] M. Fixman. Simulation of polymer dynamics. I. General theory. *J. Chem. Phys.*, 69:1527, 1978.
  - [25] P.S. Grassia, E.J. Hinch, and L.C. Nitsche. Computer simulations of brownian motion of complex systems. *Journal of Fluid Mechanics*, 282:373–403, 1995.
  - [26] R. M. Jendrejack, J. J. de Pablo, and M. D. Graham. Stochastic simulations of DNA in flow: Dynamics and the effects of hydrodynamic interactions. *J. Chem. Phys.*, 116(17):7752–7759, 2002.
  - [27] Richard M Jendrejack, David C Schwartz, Michael D Graham, and Juan J de Pablo. Effect of confinement on DNA dynamics in microfluidic devices. *J. Chem. Phys.*, 119:1165, 2003.
  - [28] J. P. Hernandez-Ortiz, J. J. de Pablo, and M. D. Graham. Fast Computation of Many-Particle Hydrody-

- namic and Electrostatic Interactions in a Confined Geometry. *Phys. Rev. Lett.*, 98(14):140602, 2007.
- [29] Yu Zhang, Juan J de Pablo, and Michael D Graham. An immersed boundary method for brownian dynamics simulation of polymers in complex geometries: Application to dna flowing through a nanoslit with embedded nanopits. *The Journal of Chemical Physics*, 136:014901, 2012.
- [30] Shidong Jiang, Zhi Liang, and Jingfang Huang. A fast algorithm for brownian dynamics simulation with hydrodynamic interactions. *Mathematics of Computation*, 82(283):1631–1645, 2013.
- [31] A. Sierou and J. F. Brady. Accelerated Stokesian Dynamics simulations. *J. Fluid Mech.*, 448:115–146, 2001.
- [32] James W. Swan and John F. Brady. Simulation of hydrodynamically interacting particles near a no-slip boundary. *Physics of Fluids*, 19(11):113306, 2007.
- [33] K Hinsén. HYDROLIB: a library for the evaluation of hydrodynamic interactions in colloidal suspensions. *Computer physics communications*, 88(2):327–340, 1995.
- [34] B Cichocki and K Hinsén. Stokes drag on conglomerates of spheres. *Physics of Fluids*, 7:285, 1995.
- [35] A Ortega, D Amorós, and J García de La Torre. Prediction of hydrodynamic and other solution properties of rigid proteins from atomic-and residue-level models. *Biophysical journal*, 101(4):892–898, 2011. Code available at <http://leonardo.inf.um.es/macromol/programs/hydropro/hydropro.htm>.
- [36] José García de la Torre, María L Huertas, and Beatriz Carrasco. Calculation of hydrodynamic properties of globular proteins from their atomic-level structure. *Biophysical Journal*, 78(2):719–730, 2000.
- [37] James W Swan and John F Brady. Particle motion between parallel walls: Hydrodynamics and simulation. *Physics of Fluids*, 22:103301, 2010.
- [38] James W Swan and John F Brady. The hydrodynamics of confined dispersions. *Journal of Fluid Mechanics*, 687:254, 2011.
- [39] Raphaël Pesché and Gerhard Nägele. Stokesian dynamics study of quasi-two-dimensional suspensions confined between two parallel walls. *Physical Review E*, 62(4):5432, 2000.
- [40] Adolfo J Banchio and John F Brady. Accelerated stokesian dynamics: Brownian motion. *The Journal of chemical physics*, 118:10323, 2003.
- [41] E. H. Hauge and A. Martin-Lof. Fluctuating hydrodynamics and Brownian motion. *J. Stat. Phys.*, 7(3):259–281, 1973.
- [42] D. Bedeaux and P. Mazur. Brownian motion and fluctuating hydrodynamics. *Physica*, 76(2):247–258, 1974.
- [43] E. J. Hinch. Application of the Langevin equation to fluid suspensions. *J. Fluid Mech.*, 72(03):499–511, 1975.
- [44] J. N. Roux. Brownian particles at different times scales: a new derivation of the Smoluchowski equation. *Phys. A*, 188:526–552, 1992.
- [45] F. Balboa Usabiaga, X. Xie, R. Delgado-Buscalioni, and A. Donev. The Stokes-Einstein Relation at Moderate Schmidt Number. *J. Chem. Phys.*, 139(21):214113, 2013.
- [46] Tri T Pham, Ulf D Schiller, J Ravi Prakash, and Burkhard Dünweg. Implicit and explicit solvent models for the simulation of a single polymer chain in solution: Lattice boltzmann versus brownian dynamics. *J. Chem. Phys.*, 131:164114, 2009.
- [47] I. Theurkauff, C. Cottin-Bizonne, J. Palacci, C. Ybert, and L. Bocquet. Dynamic clustering in active colloidal suspensions with chemical signaling. *Phys. Rev. Lett.*, 108:268303, 2012.
- [48] Jeremie Palacci, Stefano Sacanna, Asher Preska Steinberg, David J Pine, and Paul M Chaikin. Living crystals of light-activated colloidal surfers. *Science*, 339(6122):936–940, 2013.
- [49] B.E. Griffith. An accurate and efficient method for the incompressible Navier-Stokes equations using the projection method as a preconditioner. *J. Comp. Phys.*, 228(20):7565–7595, 2009.
- [50] P. J. Atzberger, P. R. Kramer, and C. S. Peskin. A stochastic immersed boundary method for fluid-structure dynamics at microscopic length scales. *J. Comp. Phys.*, 224:1255–1292, 2007.
- [51] S. Lomholt and M.R. Maxey. Force-coupling method for particulate two-phase flow: Stokes flow. *J. Comp. Phys.*, 184(2):381–405, 2003.
- [52] M. R. Maxey and B. K. Patel. Localized force representations for particles sedimenting in Stokes flow. *International journal of multiphase flow*, 27(9):1603–1626, 2001.
- [53] D Liu, EE Keaveny, Martin R Maxey, and George E Karniadakis. Force-coupling method for flows with ellipsoidal particles. *Journal of Computational Physics*, 228(10):3559–3581, 2009.
- [54] C.S. Peskin. The immersed boundary method. *Acta Numerica*, 11:479–517, 2002.
- [55] Pat Plunkett, Jonathan Hu, Christopher Siefert, and Paul J Atzberger. Spatially adaptive stochastic methods for fluid-structure interactions subject to thermal fluctuations in domains with complex geometries. *Journal of Computational Physics*, 277:121–137, 2014.
- [56] M. Hütter and H.C. Öttinger. Fluctuation-dissipation theorem, kinetic stochastic integral and efficient simulations. *J. Chem. Soc., Faraday Trans.*, 94(10):1403–1405, 1998.
- [57] Marshall Fixman. Construction of langevin forces in the simulation of hydrodynamic interaction. *Macromolecules*, 19(4):1204–1207, 1986.
- [58] Jens Rotne and Stephen Prager. Variational treatment of hydrodynamic interaction in polymers. *The Journal of Chemical Physics*, 50:4831, 1969.
- [59] A. Donev, T. G. Fai, and E. Vanden-Eijnden. A reversible mesoscopic model of diffusion in liquids: from giant fluctuations to Fick’s law. *Journal of Statistical Mechanics: Theory and Experiment*, 2014(4):P04004, 2014.
- [60] JR Blake. A note on the image system for a stokeslet in a no-slip boundary. In *Proc. Camb. Phil. Soc.*, volume 70, pages 303–310. Cambridge Univ Press, 1971.
- [61] P. J. Atzberger. A note on the correspondence of an immersed boundary method incorporating thermal fluctuations with Stokesian-Brownian dynamics. *Physica D: Nonlinear Phenomena*, 226(2):144–150, 2007.
- [62] Kyongmin Yeo and Martin R Maxey. Dynamics of concentrated suspensions of non-colloidal particles in couette flow. *Journal of Fluid Mechanics*, 649(1):205–231, 2010.
- [63] R. W. Nash, R. Adhikari, and M. E. Cates. Singular forces and pointlike colloids in lattice boltzmann hydrodynamics. *Physical Review E*, 77(2):026709, 2008.

- [64] F. Balboa Usabiaga, I. Pagonabarraga, and R. Delgado-Buscalioni. Inertial coupling for point particle fluctuating hydrodynamics. *J. Comp. Phys.*, 235:701–722, 2013.
- [65] A. Pal Singh Bhalla, B. E. Griffith, N. A. Patankar, and A. Donev. A Minimally-Resolved Immersed Boundary Model for Reaction-Diffusion Problems. *J. Chem. Phys.*, 139(21):214112, 2013.
- [66] B.E. Griffith, X. Luo, D.M. McQueen, and C.S. Peskin. Simulating the fluid dynamics of natural and prosthetic heart valves using the immersed boundary method. *International Journal of Applied Mechanics*, 1(01):137–177, 2009.
- [67] G. Tabak and P.J. Atzberger. Systematic stochastic reduction of inertial fluid-structure interactions subject to thermal fluctuations. *arXiv preprint arXiv:1211.3798*, 2013.
- [68] S. Delong, B. E. Griffith, E. Vanden-Eijnden, and A. Donev. Temporal Integrators for Fluctuating Hydrodynamics. *Phys. Rev. E*, 87(3):033302, 2013.
- [69] F. Balboa Usabiaga, J. B. Bell, R. Delgado-Buscalioni, A. Donev, T. G. Fai, B. E. Griffith, and C. S. Peskin. Staggered Schemes for Fluctuating Hydrodynamics. *SIAM J. Multiscale Modeling and Simulation*, 10(4):1369–1408, 2012.
- [70] C. W. Gardiner and M. L. Steyn-Ross. Adiabatic elimination in stochastic systems. I-III. *Phys. Rev. A*, 29:2814–2844, 1984.
- [71] Grigorios A Pavliotis and Andrew M Stuart. *Multiscale methods: averaging and homogenization*, volume 53. Springer, 2008.
- [72] A. Donev, T. G. Fai, and E. Vanden-Eijnden. Reversible Diffusion by Thermal Fluctuations. *Arxiv preprint 1306.3158*, 2013.
- [73] H Hasimoto. On the periodic fundamental solutions of the stokes equations and their application to viscous flow past a cubic array of spheres. *J. Fluid Mech*, 5(02):317–328, 1959.
- [74] Alexandre M Roma, Charles S Peskin, and Marsha J Berger. An adaptive version of the immersed boundary method. *J. Comput. Phys.*, 153(2):509–534, 1999.
- [75] Thomas Schaffter. Numerical integration of sdes: a short tutorial. *Swiss Federal Institute of Technology in Lausanne (EPFL), Switzerland, Unpublished manuscript*, 2010.
- [76] A Abdulle, G Vilmart, and K Zygalakis. Weak second order explicit stabilized methods for stiff stochastic differential equations. *SIAM J. Sci. Comput.*, 35(4):A1792–A1814, 2013.
- [77] B.E. Griffith, R.D. Hornung, D.M. McQueen, and C.S. Peskin. An adaptive, formally second order accurate version of the immersed boundary method. *J. Comput. Phys.*, 223(1):10–49, 2007. Software available at <http://ibamr.googlecode.com>.
- [78] L. Greengard and J. Lee. Accelerating the nonuniform fast fourier transform. *SIAM Review*, 46(3):443–454, 2004.
- [79] Thorben Benesch, Sotira Yiacoumi, and Costas Tsouris. Brownian motion in confinement. *Phys. Rev. E*, 68:021401, 2003.
- [80] Peter Huang and Kenneth S Breuer. Direct measurement of anisotropic near-wall hindered diffusion using total internal reflection velocimetry. *Physical review E*, 76(4):046307, 2007.
- [81] AJ Goldman, Raymond G Cox, and Howard Brenner. Slow viscous motion of a sphere parallel to a plane wall - i motion through a quiescent fluid. *Chemical engineering science*, 22(4):637–651, 1967.
- [82] Luc P. Faucheux and Albert J. Libchaber. Confined brownian motion. *Phys. Rev. E*, 49:5158–5163, 1994.
- [83] Eligiusz Wajnryb, Krzysztof A Mizerski, Pawel J Zuk, and Piotr Szymczak. Generalization of the rotne-prager-yamakawa mobility and shear disturbance tensors. *Journal of Fluid Mechanics*, 731:R3, 2013.
- [84] John C Crocker. Measurement of the hydrodynamic corrections to the brownian motion of two colloidal spheres. *J. Chem. Phys.*, 106:2837, 1997.
- [85] Lukas Holzer, Jochen Bammert, Roland Rzehak, and Walter Zimmermann. Dynamics of a trapped brownian particle in shear flows. *Physical Review E*, 81(4):041124, 2010.
- [86] Jochen Bammert, Lukas Holzer, and Walter Zimmermann. Dynamics of two trapped brownian particles: Shear-induced cross-correlations. *The European Physical Journal E*, 33(4):313–325, 2010.
- [87] Paul J. Atzberger. Incorporating shear into stochastic eulerian-lagrangian methods for rheological studies of complex fluids and soft materials. *Physica D: Nonlinear Phenomena*, 265(0):57 – 70, 2013.
- [88] C. W. J. Beenakker. Ewald sum of the Rotne-Prager tensor. *J. Chem. Phys.*, 85:1581, 1986.
- [89] A. Furukawa and H. Tanaka. Key role of hydrodynamic interactions in colloidal gelation. *Phys. Rev. Lett.*, 104(24):245702, 2010.
- [90] N. Bou-Rabee, A. Donev, and E. Vanden-Eijnden. Metropolis Integration Schemes for Self-Adjoint Diffusions. *SIAM J. Multiscale Modeling and Simulation*, 12(2):781–831, 2014.
- [91] Leslie Greengard and Mary Catherine Kropinski. An integral equation approach to the incompressible navier-stokes equations in two dimensions. *SIAM Journal on Scientific Computing*, 20(1):318–336, 1998.
- [92] Anna-Karin Tornberg and Leslie Greengard. A fast multipole method for the three-dimensional stokes equations. *Journal of Computational Physics*, 227(3):1613–1619, 2008.
- [93] Eric E Keaveny and Michael J Shelley. Applying a second-kind boundary integral equation for surface tractions in stokes flow. *Journal of Computational Physics*, 230(5):2141–2159, 2011.
- [94] D. Devendran and C. S. Peskin. An immersed boundary energy-based method for incompressible viscoelasticity. *J. Comp. Phys.*, 231(14):4613–4642, 2012.
- [95] G.N. Milstein and M.V. Tretyakov. *Stochastic numerics for mathematical physics*. Springer, 2004.
- [96] Y. Zhang, A. Donev, T. Weisgraber, B. J. Alder, M. D. Graham, and J. J. de Pablo. Tethered DNA Dynamics in Shear Flow. *J. Chem. Phys.*, 130(23):234902, 2009.
- [97] B.E. Griffith and S. Lim. Simulating an elastic ring with bend and twist by an adaptive generalized immersed boundary method. *Commun. Comput. Phys.*, 12:433–461, 2012.
- [98] S. Lim, A. Ferent, X. S. Wang, and C. S. Peskin. Dynamics of a closed rod with twist and bend in fluid. *SIAM J Sci Comput*, 31(1):273–302, 2008.
- [99] Note that the mobility is symmetric so there is no notational ambiguity in  $\partial_{\mathbf{q}} \cdot \mathbf{M}$ .
- [100] Note that this is an approximation and in practice the mobility is not pairwise additive if higher-order multi-

poles such as stresslets are accounted for, see Appendix B.

- [101] Perhaps a more relevant diffusive length scale to use is the typical inter-particle gap, which can be substantially smaller than  $a$  for dense suspensions.
- [102] In Green's function's based approaches there is no difficulty in dealing with unbounded three dimensional systems (at rest at infinity) since the Oseen tensor is the required response function and is easy to compute. Note

however that when simulating periodic domains (e.g., colloidal suspensions) one requires the Green's functions for Stokes flow in a periodic domain, and these are *not* simple to compute [28, 88], unlike in our approach, which handles boundary conditions naturally.

- [103] Note, however, that Metropolisization of even the simple midpoint scheme is a rather nontrivial task because the mobility matrix is never formed or factorized in FIB.